Article:
Gao, W. orcid.org/0009-0007-7929-2315, Cheng, Z., Gregory, D.A. et al. (5 more authors) (2025) Advancing synthetic bone tissue engineering materials: Nano-scale investigation into transitional Interface in carbon dots/ polymer composites. Journal of Colloid and Interface Science, 700 (Part 3). 138553. ISSN: 0021-9797

https://doi.org/10.1016/j.jcis.2025.138553

Advancing Synthetic Bone Tissue Engineering Materials: Nano-scale Investigation into Transitional Interface in Carbon Dots/ Polymer Composites

Woming Gao[1], Zeming Cheng[1,2], David A. Gregory[1,2], Alexander J. Knight[3], Alexander I. Tartakovskii[3], Cornelia Rodenburg[1,2]*, Nicholas T.H. Farr[1,2]*, Frederik Claeyssens[1,2]*

* Corresponding authors

[1] School of Chemical, Materials and Biological Engineering, Sir Robert Hadfield Building, University of Sheffield, Sheffield, S1 3JD, UK

[2] Insigneo Institute for in Silico Medicine, Pam Liversidge Building, University of Sheffield, S1 3JD, UK

[3] School of Mathematical and Physical Sciences, Hicks Building, University of Sheffield, Sheffield, S3 7RH, UK

Keywords: carbon dots, nano-scale spectroscopy, transition interface layer, vat photopolymerisation, nano composite, 3D-printable bone tissue engineering material

Abstract

Identifying suitable biocompatible and processable materials that mimic the properties of native bone tissue remains a significant challenge in bone tissue engineering (BTE). Polymerized Trimethylolpropane Triacrylate (PTMPTA), a rapid photocurable, stiff, bioinert thermoset polymer, has previously suggested as matrix of BTE composites, but still lacks mechanical properties, biocompatibility, and printing accuracy, which need to be improved to meet BTE requirements. In this study, citric acid carbon dots (CA CDs) synthesized via microwave pyrolysis were blended into the PTMPTA matrix. Nano-scale spectroscopy and atomic force microscopy (AFM) techniques for the first time revealed the transitional interface layers with different chemical structures between CA CDs and PTMPTA. Those transitional interface layers facilitate uniform stress distribution, enhance load transfer, prevent debonding caused by CDs agglomeration, reduce over-curing and thermal stress and improving surface cell adhesion and proliferation, together with CA CDs enhancing mechanical strength, biocompatibility, and processability of the resulting composite. Ultimately, composite incorporating 8 wt% CA CDs was determined to the highest mechanical properties, biocompatibility, and 3D printing accuracy, achieving a 3.5-fold increase in compressive Young's modulus and load-bearing capacity, a 1.5-fold increase in tensile Young's modulus, and a 2-fold cell surface proliferation compared to pure PTMPTA, and has successfully approached the target 3D printing accuracy. This work opens the door to the vast compositional space of different carbon dot/polymer composites targeting the demanding requirements of BTE and lays the foundation for future BTE materials.

1. Introduction

Developing polymers that exhibit both high strength and biocompatibility remains a significant challenge, particularly for bone tissue engineering (BTE) applications. Bones not only support and protect the human body structure but also withstand impact forces during movement [1], [2]. Therefore, materials selected for BTE must replicate the natural properties of bone, ensuring high mechanical strength and optimal biocompatibility to support cell adhesion and growth [3], [4]. Additive manufacturing, particularly vat photopolymerization, has emerged as a powerful method for precisely replicating bone tissue architecture in BTE [5]. Consequently, materials for 3D printing must support high-resolution printing to fabricate intricate, fine structures.

Polymerized trimethylolpropane triacrylate (PTMPTA) is commonly used as a matrix material or a crosslinking agent. Trimethylolpropane triacrylate (TMPTA) is a monomer featuring three acrylic functional groups, enabling rapid cross-linking under UV light in the presence of a photoinitiator, within a few seconds [6], [7], [8]. PTMPTA is known for its rapid photocuring, curing strong wear resistance and bioinert properties [9], [10], [11], however, pure PTMPTA and its copolymers exhibit limitations in terms of wettability and mechanical strength, both of which are crucial for BTE [9], [12], [13]. Additionally, PTMPTA's 3D printing precision is low because of the rapid curing [14], pose challenges for ideal BTE 3D-printing scaffolds.

Carbon dots (CDs), a class of nanomaterials first synthesized by Xu *et al.* in 2004 [15], have gained attention for their unique optical properties, simple synthesis, low cost, broad precursor selection, excellent biocompatibility, and tuneable surface characteristics [16], [17], [18]. Previous studies have shown that blending CDs with polymers can enhance mechanical properties and biocompatibility of the resulting polymer composites. For example, Gogoi *et al.* created CD-PU-HA (carbon dots-polyurethane-hydroxyapatite) composites that demonstrated favourable mechanical properties and promoted high cell proliferation and alkaline phosphatase (ALP) activity in MG-63 osteoblastic cell lines [19]. CDs have also been shown to improve the accuracy of 3D printing. For instance, Liang *et al.* incorporated CDs into hydrogel-based 3D printing, resulting in enhanced dimensional accuracy [20]. However, at present, the combination of PTMPTA and CDs has not been investigated, and further to our knowledge no study has clearly demonstrated how carbon dots and polymers affect each other at the nanoscale in a composite.

In this study we synthesized citric acid carbon dots (CA CDs) via microwave pyrolysis of citric acid and blended them with TMPTA to form novel CA CDs/PTMPTA composites. Different proportions of CA CDs were added to evaluate their impact on the mechanical properties, biocompatibility, and 3D printing accuracy of the resulting scaffolds. We found the composites, especially containing 8% CA CDs, exhibited enhanced performance compared to PTMPTA. Utilizing nanoscale spectroscopy and atomic force microscopy techniques, we visually identified, for the first time, the formation of transitional interface layers with different chemical structure between CA CDs and PTMPTA, which was found to be a key factor contributing to the improved properties of the composite material.

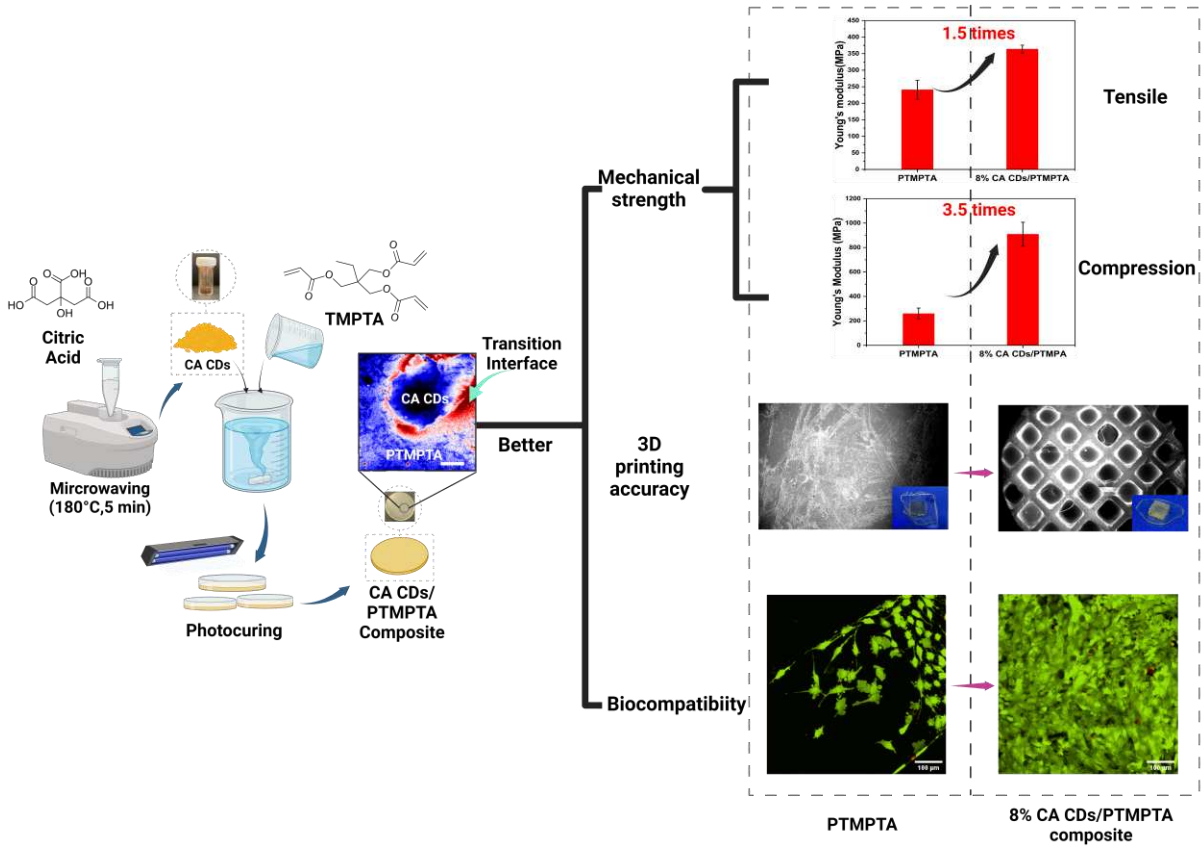

Figure 1. An overview of the production process of CA CDs/PTMPTA composites and how the transition interface layer between CA CDs and PTMPTA affects the composites.

2. Results and Discussion

To obtain CA CDs, citric acid was initially pyrolyzed, and the resulting product was purified. X-ray Diffraction Spectroscopy (XRD), Transmission Electron Microscopy (TEM), Ultraviolet-visible (UV-VIS) absorption spectroscopy, fluorescence emission spectroscopy, and Dynamic Light Scattering (DLS) analysis were conducted to confirm the purity of the incorporated CA CDs.

The XRD pattern of unpurified CA CDs (black curve) and CA CDs after purification (red curve) are shown in Figure 2A. The pattern of the unpurified CA CDs resembled that of citric acid, displaying numerous narrow, high-intensity crystallization peaks [21]. In contrast, the pattern for purified CA CDs only exhibited a large, broad peak spanning around 22° and 43°, which corresponds to the characteristic peaks of CDs [22]. The comparison of the two curves demonstrates that the purification process effectively removed most small molecular impurities while retaining the CA CDs. The TEM image (Figure 2B) displays spherical CA CDs particles with diameter around 2-7 nm (inset in Figure 2B). The High-resolution transmission electron microscopy (HRTEM) image and its fast Fourier transformation (FFT) image further reveal distinct lattice fringes in single particles, exhibiting a spacing of 0.21 nm (Figure 2C), which is characteristic of CDs [23], [24]. The fringes appear slightly distorted and wavy, which could be due to strain or defects in the carbon dot (CD) structure. In addition, not all CD particles remained isolated, as they were prone to agglomeration. DLS characterization identified four distinct particle size distributions of 8 wt% CDs in TMPTA (Figure 2D): particles smaller than 10 nm, aggregates ranging from 10-40

nm, larger clusters measuring 50-1000 nm and very large aggregates exceeding 1 micron. These findings suggest that CDs readily form agglomerates of varying sizes. The absorption spectrum (red curve in Figure 2E) exhibited two peaks, one below 300 nm and one around 340 nm, corresponding to the π-π* and n-π* transitions of carbon dots, respectively [25], [26]. Additionally, the emission spectrum (blue curve in Figure 2E) displays the typical photoluminescence characteristics of CDs. Further information of synthesis and characteristics of CA CDs are provided in the supplementary information (Figure S1-S2, Table S1).

The purified CA CDs were mixed with the TMPTA monomer resin, at the mass ratios of 0%, 2%, 4%, 6%, 8% and 10% to TMPTA. Following the curing process under 365 nm UV light for 90 s, the resulting composites were designated as from 2% to 10% CA CDs/PTMPTA composite. The detailed synthesis process of composites is illustrated in the supporting information (Figure S3).

Fourier Transform Infrared Spectroscopy (FTIR) and XRD spectroscopy were conducted to verify whether the CA CDs were effectively blended into the PTMPTA matrix. The FTIR spectrum of CA CDs/PTMPTA composites and the PTMPTA is shown in Figure 2F. The peak intensity at 2920 and 2850 cm^{-1} increased in line with the concentration of CA CDs, corresponding to the C-H stretching vibrations of methylene and methyl groups [27] (Figure S5A). These peak changes suggest that as the concentration of CDs increases, the contribution of surface functional groups of CA CDs, such as alkyl or aliphatic groups, to the FTIR spectrum becomes more pronounced. However, the intensity of the CH bending vibration near 1460 cm^{-1} did not increase proportionally with the rise in CD content (Figure S5B). This phenomenon may be attributed to the incomplete dispersion of carbon dots within the composite material, with this peak primarily corresponding to methylene signals at PTMPTA cross-linking sites [28]. Similarly, the signal near 3440 cm^{-1} increased and broadened, which is associated with hydroxyl groups of CDs and further indicates possible hydrogen bonding interactions between CDs and PTMPTA [29] (Figure S5C). Simultaneously, the intensity of the peak at 1720 cm^{-1}, corresponding to the -C=O bond in PTMPTA, decreased (Figure S5D) [30]. This reduction might result from the activation of carbonyl (-C=O) surface groups via photoinitiation, leading to the production of ether crosslinks with TMPTA monomers. This suggests that some CA CDs were grafted onto PTMPTA [31], resulting in the observed enhancement of the C-O peak at 1115 and 1260 cm^{-1} (Figure S5E) [32], [33].

The XRD spectra of various CA CDs/PTMPTA composites and pure PTMPTA is displayed in Figure 2G. The XRD curve of PTMPTA (black curve) exhibits a broad amorphous peak between 10° and 30°, indicating the amorphous structure of PTMPTA. After blending PTMPTA with CA CDs, this peak remains present, while the sharp peaks around $2\theta = 23°$ exhibit slight shifts to higher values, potentially corresponding to the crystalline regions contributed by the CDs. Additionally, when the CDs content reaches 6% or more, several additional weak peaks or subtle features emerge in the composite material, indicating changes in crystallization. Combined with the FTIR results, the broadening and increased intensity of the OH stretching region (3440 cm^{-1}) suggests the formation of hydrogen bonds. Those hydrogen bonds may enhance chain arrangement, act as nucleation points, and influence crystallization [34]. The CH stretching vibrations (2925 and 2853 cm^{-1}) and the introduction of C-O groups (1260 cm^{-1}) further illustrate interactions or entanglements between molecular chains and CDs, which could affect polymer chain alignment and alter crystallization. In the SEM image of the 8% CA CDs/PTMPTA composite (Figure 2H), individual CDs on the surface were too small to be resolved; however, agglomerated CDs are clearly identifiable. These agglomerates range in size from 80 to 320 nm within the PTMPTA matrix (Figure

2I, results based on counting in Figure 2H). All the above characterisations confirm the incorporation of CA CDs into PTMPTA. Additionally, the FTIR and XRD results indicate that CA CDs interact with PTMPTA, which is likely to influence its structural and functional properties.

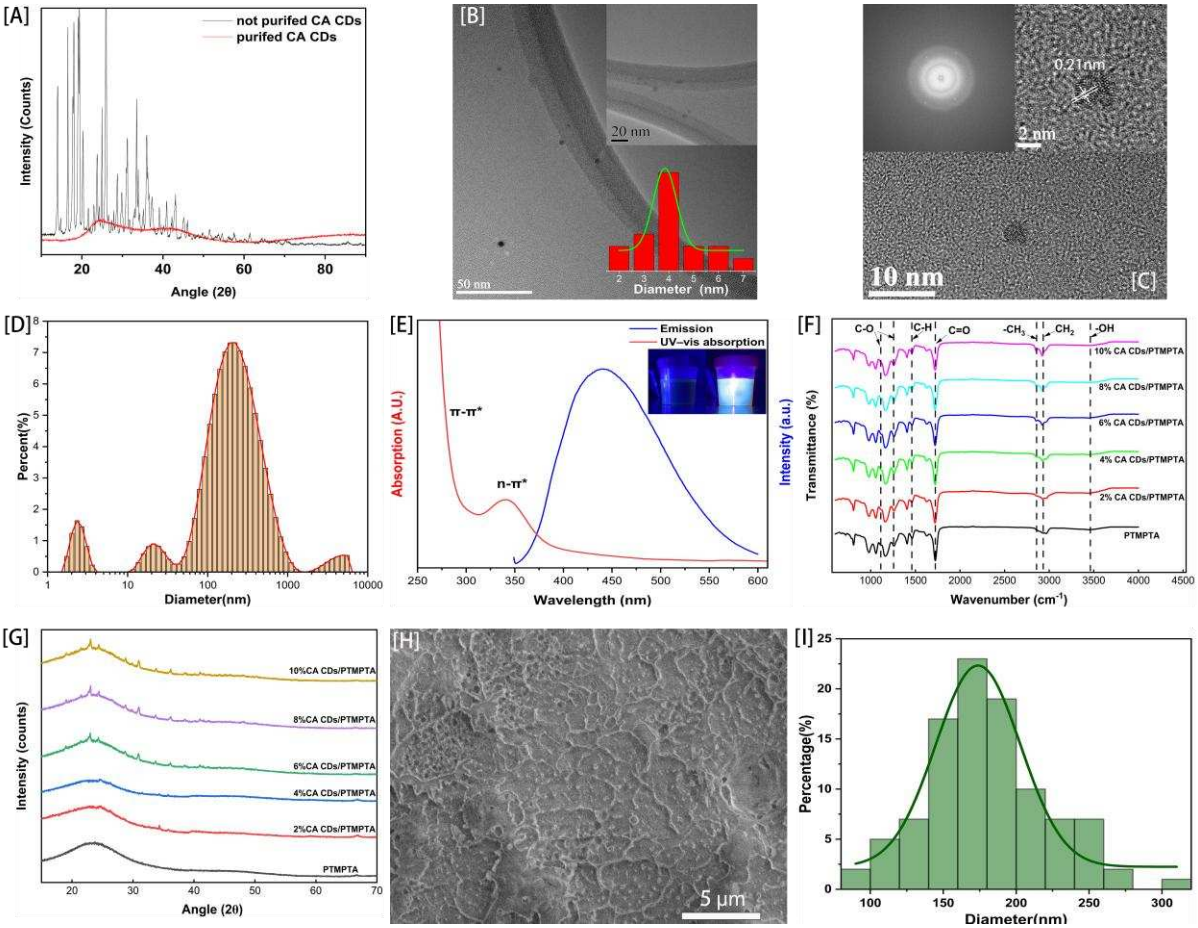

Figure 2. (A) XRD patterns of unpurified (black curve) and purified CA CDs (red curve). (B) TEM image of CA CDs with a scale bar of 50 nm. Inset: up: TEM image with a scale bar of 20 nm, below: the corresponding particle size histogram. (C) HRTEM image of single CA CD with a scale bar of 10 nm. Inset: left: FFT of this CA CD, right: size of lattice fringes of a single CA CD with a scale bar of 2 nm. (D) DLS result of CA CDs, show four ranges of particle size: less than 10 nm; 10-40 nm; 50-1000 nm and above 1000 nm. (E) The absorption spectrum (red curve) and the fluorescence emission spectrum (blue curve) excitation at 340 nm of CA CDs water solution. Inset: the fluorescence of the CA CDs water solution under a 365 nm UV lamp. (F-G) FTIR and XRD spectra of PTMPTA polymer and CA CDs/PTMPTA composites. (H) SEM image of 8% CA CDs/PTMPTA composites with a scale bar of 5 μm. (I) According to the SEM images, the particle size distribution of 100 particles was measured.

To investigate the impact of CA CDs on the strength properties of PTMPTA, both tensile and compression tests were conducted. In the tensile test, 10 samples of each composite and PTMPTA polymer were measured, and the average values were calculated for comparison (Table S2). The results indicate that when the CA CDs content was below 6 wt% in the composite, their concentration had a positive correlation with the composite's Young's modulus (Figure 3A). However, this trend reversed once the CA CDs content surpassed 8 wt%. This phenomenon may

be explained by the precipitation of CA CDs at higher concentrations, which caused the mixture to become more heterogeneous (Figure S3C). This heterogeneity led to stress concentration and inconsistent stress distribution in various regions, ultimately deteriorating the composite's mechanical properties. The tensile Young's moduli of all CA CDs/PTMPTA composites were significantly higher than that of the PTMPTA polymer. Prior to exceeding an incorporation level of 8% CA CDs, an increase in CA CDs content resulted in a corresponding increase in the modulus.

The compression test results are shown in Figures 3B-C. Each type of composite was tested with 5 replicates, and the average data obtained were used for comparison (Tables S3-S4). For CA CDs content up to 8 wt%, an increase in the CA CDs proportion resulted in a higher load-bearing capacity (Figure 3B) and Young's modulus (Figure 3C), indicating enhanced compressive strength with increasing CA CDs concentration. However, when the proportion of CA CDs reached 10 wt%, the load-bearing capacity and Young's modulus of 10% CA CDs/PTMPTA composites significantly decreased. This reduction is likely caused by the opacity introduced by higher CA CDs concentrations, which prevented UV light penetration and resulted in incomplete crosslinking of the composites. Consequently, some interior parts of the sample remained liquid, significantly compromising the mechanical properties of the composites. Both tensile and compression tests demonstrated that CA CDs significantly enhanced the mechanical properties of the polymer matrix. Among all compositions, the composite containing 8% CA CDs are the most suitable candidates for BTE, with the tensile Young's modulus increasing by around 1.5 fold (363.70 ± 11.96 MPa) compared to pure PTMPTA (240.78 ± 28.42 MPa). Additionally, the compressive Young's modulus and maximum load-bearing capacity increased by around 3.5 fold (18.70 ± 1.32 kN and 908.68 ± 98.10 MPa) to pure PTMPTA (5.39 ± 0.55 kN and 259.19 ± 45.60 MPa).

To investigate the mechanism by which CA CDs enhanced the mechanical properties, Nuclear Magnetic Resonance (NMR) analysis was conducted. Based on previous FTIR and XRD results (Figures 2F and 2G), the initial hypothesis was that interactions between CA CDs and PTMPTA might increase the crosslinking density, thereby improving the mechanical properties. To test this, the composites and PTMPTA were immersed in toluene overnight, and the excess solvent was removed by gravity filtration. Subsequently, deuterated chloroform ($CDCl_3$) was used to soak the composites for several hours before performing ^{1}H NMR analysis. The ^{1}H NMR spectra of all the composites exhibited resonance in two distinct regions (Figure 3D): a methyl signal around 2.4 ppm and an aromatic ring signal near 7.2-7.3 ppm, corresponding to resonances produced by toluene molecules absorbed by the composites. According to previous study [35], there is linear relationships between chemical displacement and the degree of solvent expansion, a shift of these signals upfield (towards smaller PPM values) indicates an increase in crosslinking density. Due to significant overlap and complexity in the aromatic signals (Figure 3F), the methyl signals were chosen for detailed analysis (Figure 3E).

As shown in Figure 3E, compared to PTMPTA, the methyl signals of 2%, 4%, and 6% CA CDs/PTMPTA composites shifted slightly upfield, indicating that CA CDs promoted the crosslinking of composites to some extent. However, the methyl signals of the 8% and 10% CA CDs/PTMPTA composites shifted back downfield, with the signals of the 10% CA CDs/PTMPTA composites showing an even greater downfield shift than neat PTMPTA. These results suggest that an excessive amount of CA CDs may reduce the crosslinking density, likely due to the aggregation of CA CDs, which could impede the formation of the crosslinking network. While this analysis showed that CA CDs do influence the crosslinking of the composites, the observed signal shifts were

minimal (less than 0.1 PPM), indicating only slight changes in the crosslinking density. Furthermore, although the crosslinking density slightly decreased in the 8% CA CDs/PTMPTA composites, the compression test still exhibited the highest strength. The comparison of the NMR and compression test measurements suggests that crosslinking density had only a minor effect on the overall mechanical properties.

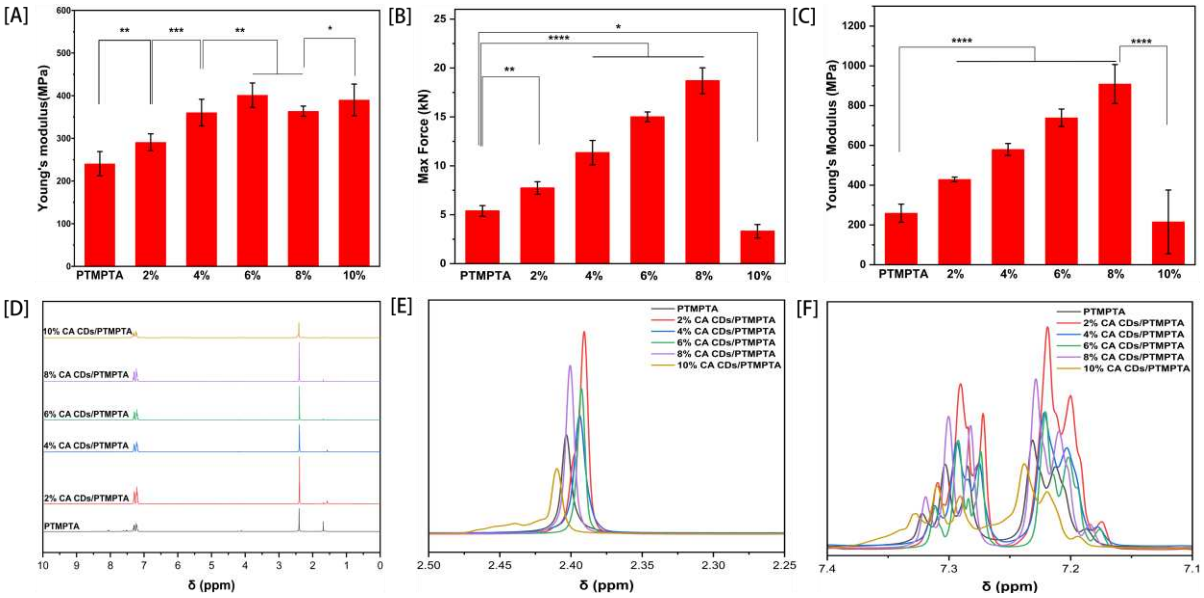

Figure 3. Tensile test data of PTMPTA and CA CDs/PTMPTA composites: (A) Tensile Young's modulus of PTMPTA and CA CDs/PTMPTA composites, all data differences are significant (n = 10; *p < 0.05). Compression test data of PTMPTA and CA CDs/PTMPTA composites: (B) Max force and (C) compression young's modulus, all data differences are significant (n = 5; *p < 0.05) and all composite materials are abbreviated as 2%, 4%, 6%, 8% and 10%. ^{1}H NMR spectra (D) of PTMPTA and CA CDs/PTMPTA composites treated with toluene recorded in $CDCl_3$, which shows two signal areas: (E) Aromatic proton resonances interval and (F) methyl proton resonances interval.

Next, the surface morphology of the 8% CA CDs/PTMPTA composite was analysed using atomic force microscopy (AFM) to investigate the distribution of CA CDs within PTMPTA and their potential impact on mechanical strength (Figure 4). Figure 4A presents a Derjaguin-Muller-Toporov (DMT) Modulus map, where brighter regions correspond to areas with a higher DMT modulus, ranging from a few nanometres to over 400 nm in diameter. When correlated with CA CDs observations from TEM, DLS and SEM (Figures 2B, 2D, and 2H), these regions were identified as CA CDs and their aggregates (the modulus up to 1.3 GPa). The DMT modulus map revealed significant spatial variation within the composite, which was segmented into three distinct regions for further analysis (Figures 4B, 4C, and 4D). In Figure 4B, areas with a modulus below 400 MPa were attributed to PTMPTA. Figure 4C identified regions corresponding to CA CDs, characterised by a modulus exceeding 480 MPa. Figure 4D highlighted intermediate-modulus regions, suggesting the presence of an interface layer with a slightly different modulus between the CA CDs and PTMPTA. To explore the interaction between CA CDs and PTMPTA, the interface structures observed in Figure 4D were examined in relation to the CA CDs in Figure 4C. Figure 4E and its inset show an overlay of Figures 4C and 4D, confirming that the intermediate-modulus regions in Figure 4D are

located around the CA CDs. This observation supports the presence of a transitional interface layer between the carbon dots and the PTMPTA matrix. Additionally, Figure 4F illustrates surface roughness, demonstrating that the incorporation of CA CDs resulted in a rougher composite surface, the average roughness (Ra) and root mean square roughness (Rq) are 11.3 nm and 7.7 nm, respectively.

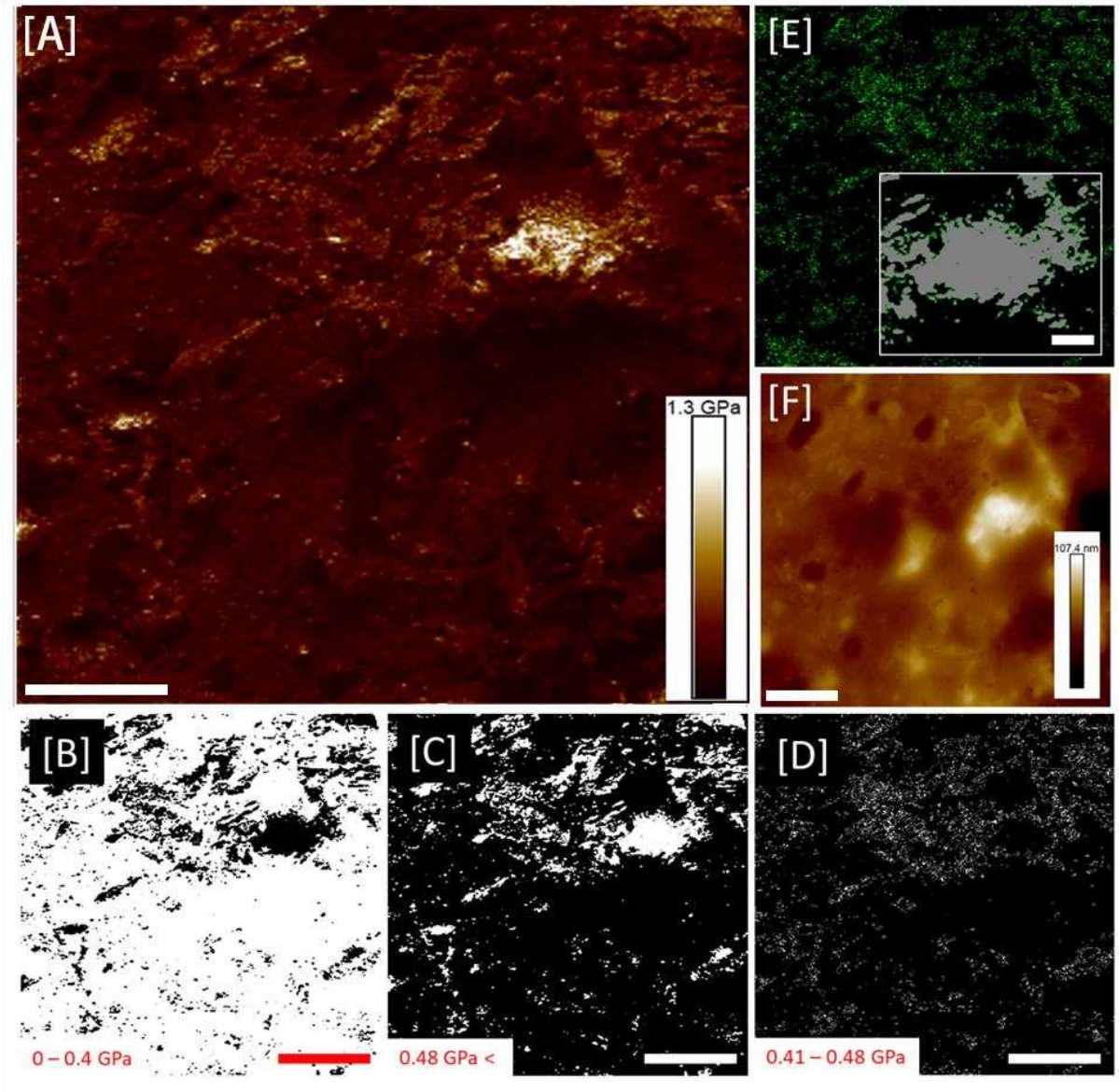

Figure 4. (A): DMT Modulus map of surface of 8% CA CDs/PTMPTA composites, with whiter colour indicating higher modulus (up to 1.3 GPa); (B-D): Binary images representing the modulus map in (A) set to the following thresholds: (B) 0.0-0.4 GPa, (C): more than 0.48 GPa, (D): 0.41-0.48 GPa. (E) and its inset: overlay between (C) and (D). (F): AFM height data showing the surface roughness of 8% CA CDs/PTMPTA composites. Ra and Rq are 11.3nm and 7.7nm, respectively. Scale bar of figure E is 100 nm, the others are 400 nm.

To further investigate the presence of an interface layer through differing chemistries, nano-Fourier transform infrared spectroscopy (nano-FTIR) and scattering-type scanning near-field optical microscopy (s-SNOM) were employed to image the CA CDs and their surroundings (Figure

5A-D). These two techniques use the illumination of a metal-coated AFM cantilever in order to generate a confined, near-field optical probe with spatial size similar to that of the cantilever tip apex (around 10 nm). As a result, these techniques can chemically characterise the PTMPTA polymer on the length scale of the CA CDs themselves, allowing us to directly probe and visualize the chemistry of the interface layer. Nano-FTIR spectra of three regions - PTMPTA polymer, CA CDs, and the interface between the two - are shown in Figure 5A, where the nano-FTIR phase data values correlate to the amount of absorption in the sample, thereby revealing the underlying chemical differences between the CA CDs, the PTMPTA, and the interface layer between them. Peaks corresponding to C-O bonds at 1115 and 1260 cm^{-1}, shared by CA CDs and PTMPTA, were significantly stronger at the interface. Conversely, the C=O peak around 1730 cm^{-1} was weaker at the interface compared to PTMPTA.

These findings indicate the formation of a chemically distinct transition interface layer, likely involving covalent ether linkages formed via reactions between CA CDs and PTMPTA. These results align with the trends observed in the FTIR spectrum of the composite (Figure 2F), indicating that the interaction between CA CDs and PTMPTA leads to the modification of C=O bonds in PTMPTA and the formation of additional C-O bonds. This chemical interaction facilitates the development of the interface layer between CA CDs and PTMPTA. This interfacial reaction likely contributes to the development of the intermediate-modulus interface layer observed in modulus mapping. Furthermore, the formation of this interface layer provides insight into the changes in crystallinity observed in the XRD spectrum (Figure 2G). The restricted arrangement of polymer chains and the altered crystal growth direction likely contribute to the observed variations in crystallinity [36]. The AFM height image (Figure 5B) and corresponding s-SNOM amplitude scan taken at 1115 cm^{-1} (Figure 5C) clearly show the presence of CA CDs and the aggregates in the composite. Figure 5D presents the corresponding phase data taken during the same 1115 cm^{-1} wavenumber s-SNOM scan and starkly highlights the chemical difference between the interface layer and both the CA CDs and the PTMPTA. Red data values in Figure 5D represent regions of stronger absorption at 1115 cm^{-1} and are therefore regions attributed to an increased density of C-O bonds. Notably, the interface layer was observed not only around larger agglomerates but also at the nanoscale, demonstrating that both individual CA CDs and their agglomerates interact with PTMPTA to form an interface.

It can be concluded that CA CDs enhance the mechanical strength of PTMPTA not only by introducing their inherently high modulus but also through the formation of a transition interface layer resulting from their interaction with PTMPTA. This interface layer may act as a buffer, enabling more uniform stress distribution between different materials and preventing stress concentration at the boundaries that could lead to failure [37]. The transition interface layer could also improve the bonding between CA CDs and the PTMPTA matrix, modifying the crystallinity, facilitating better load transfer, and preventing debonding, thereby significantly enhancing the overall mechanical properties of the composite [38]. Additionally, agglomerates within a polymer matrix may typically result in voids or defects that could lead to slipping or detachment under pressure, while the interface layer ensures a tight integration of the polymer matrix around the CA CDs, minimizing void formation and preventing premature failure under load [39]. This interface layer may also stabilize the aggregated CA CDs, preventing them from sliding or detaching under pressure, thereby allowing the aggregates to contribute positively to the overall mechanical properties of the composite.

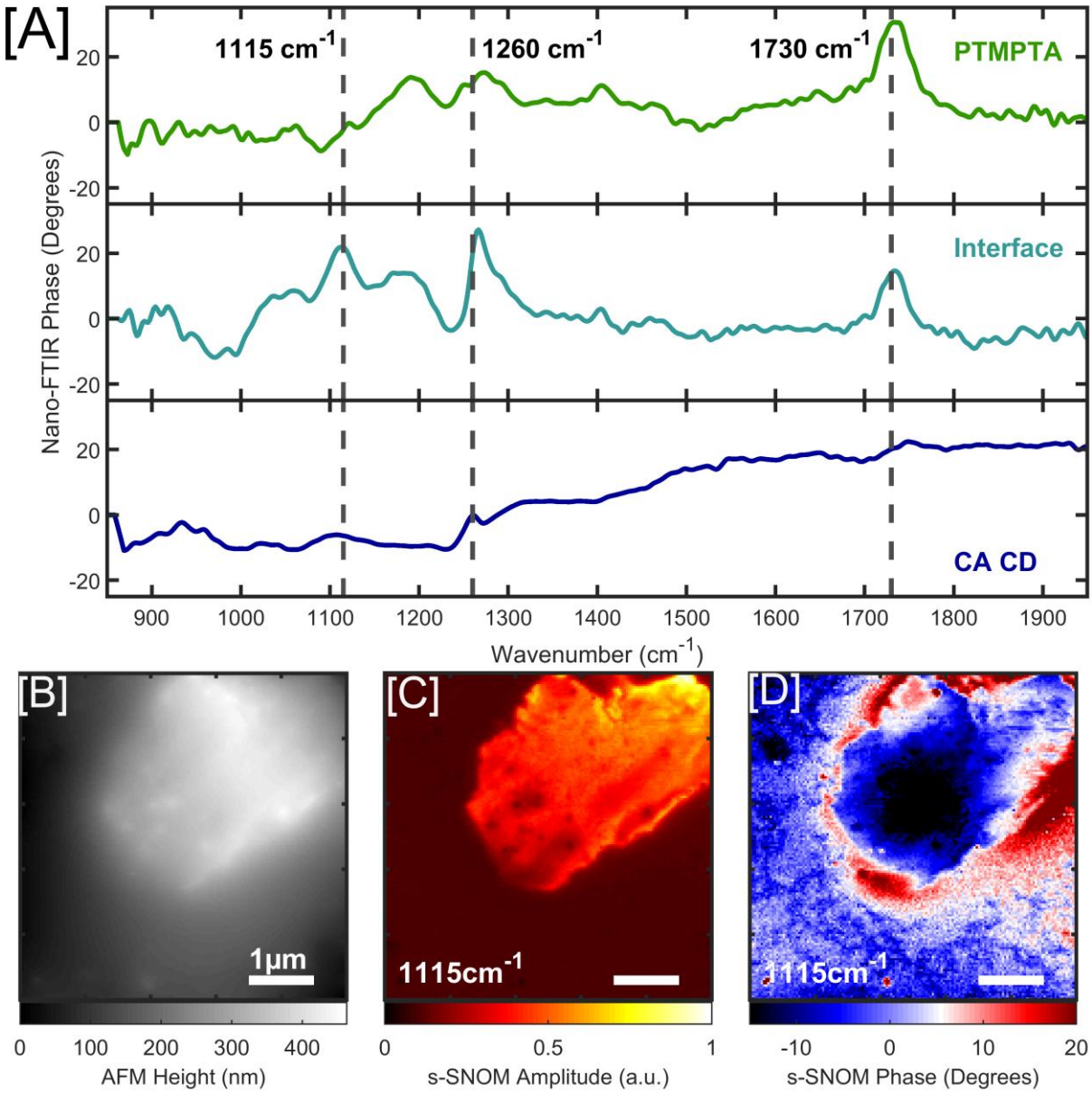

Figure 5. (A) Nano-FTIR spectra corresponding to (from top to bottom): a plain PTMPTA region, an interface region between CA CDs and PTMPTA, and CA CDs. (B-D) An s-SNOM scan taken of CA CDs and their agglomerates partially imbedded in the PTMPTA composite at wavenumber 1115 cm^{-1}, with the corresponding AFM (B), s-SNOM amplitude (C), and s-SNOM phase (D) data. The red areas in (D) highlight regions that absorb more strongly at 1115 cm^{-1}, attributed to a higher density of C-O bonds. All scale bars are 1 μm.

In addition to enhancing mechanical strength, the transition interface layer formed between CA CDs and the PTMPTA matrix may also influence the degradation behaviour of the composites by introducing sites susceptible to hydrolytic or oxidative cleavage. To evaluate this, in vitro degradation tests were conducted by immersing cured composite discs in PBS (simulating physiological conditions) and 3% H_2O_2 solution (simulating oxidative degradation) at 37 °C for 14 days. As shown in Figure 6A, PTMPTA exhibits minimal degradation in both PBS and H_2O_2 solutions, remains 99.62% and 99.35% mass after 14 days, respectively. In contrast, upon incorporation of CA CDs, the composites showed slightly increased mass loss, with the 10% CA

CDs/PTMPTA composite retaining 96.98% of its mass in PBS and 93.01% in H_2O_2, indicating that the overall degradation remained low but became more sensitive to oxidative conditions. This behaviour can be attributed to the ether bonds formed during the formation of the transition interface layer. These bonds are vulnerable to oxidative cleavage. Supporting evidence from FTIR analysis (Figure 6B) shows a reduction in the C-O stretching band intensity and a concurrent increase in the C=O band after degradation, confirming ether bond cleavage. As more CA CDs are incorporated, a greater number of ether bonds form, leading to more pronounced degradation and spectral changes. These results demonstrate that CA CDs/PTMPTA composites exhibit adjustable degradability and potential bioabsorbability.

The swelling behaviour and biocompatibility of the composites are also critical for their suitability in BTE. All formulations exhibited relatively low swelling rates (Supplementary Figure S4), remaining below 50% in deionized water, PBS, and ethanol, thereby demonstrating adequate dimensional stability [40]. Excessive swelling could otherwise compromise the structural integrity of implants [41]. The impact of CA CDs on the biocompatibility of PTMPTA was evaluated through cell viability tests and live/dead assays. For the cell viability test, MG63 cells were seeded and cultivated for 7 days on PTMPTA and CA CDs/PTMPTA composites. The cells on samples containing 2 to 8 wt% CA CDs showed significantly higher metabolic activity compared to cells on PTMPTA and 10 wt% CA CDs samples. On the seventh day, cells on the 8 wt% CA CDs samples exhibited the highest cell viability (the cell viability increasing almost 2 times compared to that on pure PTMPTA) (Figure 6C). The results were analysed using two-way Analysis of Variance (ANOVA), and cell viability on the 8 wt% CA CDs samples was significantly 2 times higher than on samples without CA CDs and those with 10 wt% CA CDs (both $^*p < 0.0001$). In contrast, there was no significant difference in cell viability between the 8 wt% CA CDs samples and tissue culture plastic (TCP), indicating that the composites supported cell growth and proliferation to a similar extent as TCP.

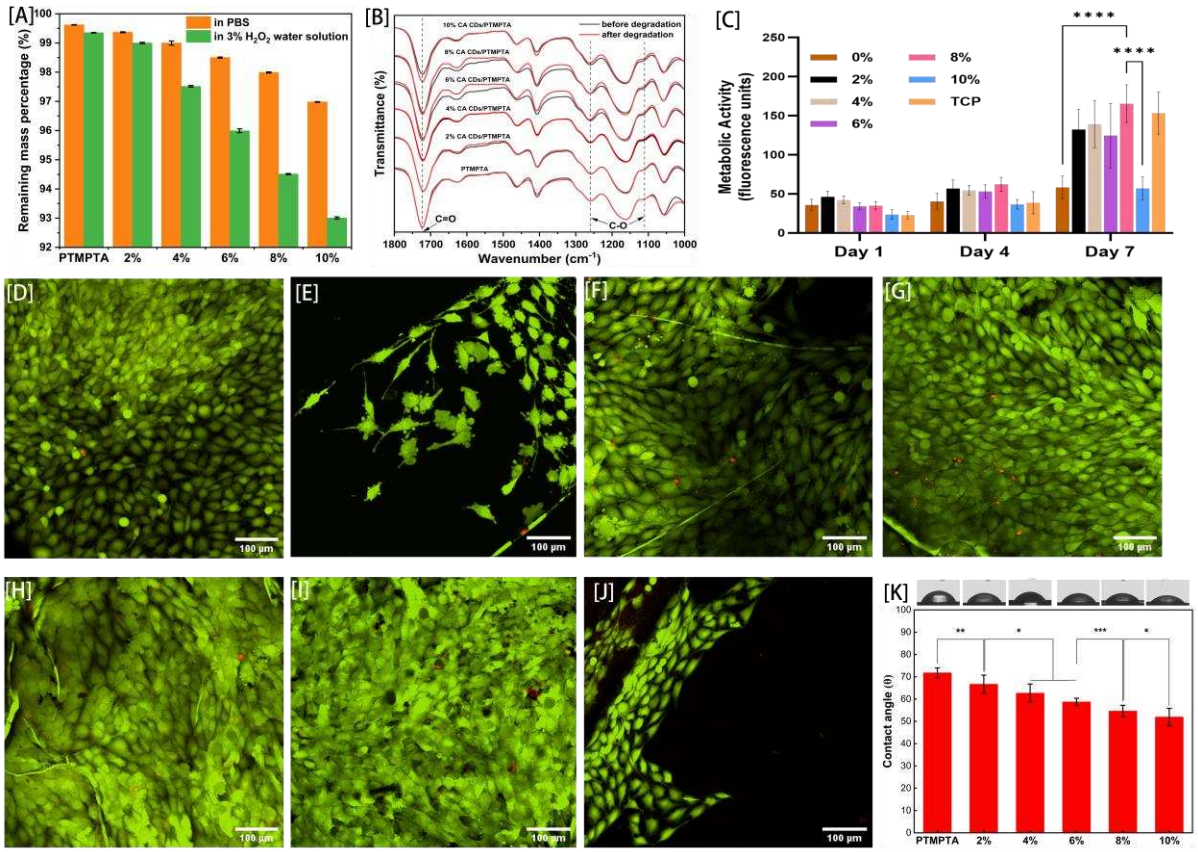

Figure 6. The remaining mass percentage results of PTMPTA and all composites (A) after 14 days degradation in PBS and 3% H_2O_2 solution, all composite materials are abbreviated as 2%, 4%, 6%, 8% and 10%. (B) is the FTIR spectra of PTMPTA and all composites before and after degradation. The resazurin assay result of cell viability (C) on day 1,4, 7 and confocal images of TCP (D), composites with CA CDs ranging from 0 wt% to 10 wt% (E)-(J), respectively on day 7. Scale bar of all figures is 100 μm. (K) is water contact angle of CA CDs/PTMPTA composites and PTMPTA. Top of the figure shows the droplet shapes contacted with different surfaces. Below shows the comparison of surface water contact angle, all composite materials are abbreviated as 2%, 4%, 6%, 8% and 10%. The water contact angle differences between all CA CDs/PTMPTA and PTMPTA were significant (mean ± SEM, n = 10 independent experiments, *p value < 0.05).

For the live/dead assay (Figure 6D-J), MG63 cells were stained with Calcein Green AM/ethidium bromide phosphate buffer solution (PBS) and observed at 10× magnification under a Nikon A1 confocal microscope after 7 days of cultivation on the sample discs. Single images were processed and combined using z-stack images of each sample. Live MG63 cells were stained bright green by Calcein Green AM, and the cells on samples containing 2 to 8 wt% CA CDs/PTMPTA composites showed high levels of viability, similar to cells on tissue culture plastic (TCP). In contrast, cells on PTMPTA and 10 wt% CA CDs/PTMPTA composites were less distributed and attached, which corresponded to the previous cell viability test results. Dead cells, stained red by ethidium bromide, were not observed in large quantities.

Combining the results of the cell proliferation test and live/dead assay, it can be concluded that PTMPTA is not suitable for cell growth. When the ratio of CA CDs was 8 wt% or less, cell growth improved progressively with the increasing CA CDs weight proportion. The AFM height image

(Figure 4F) shows that the introduction of CA CDs increased the surface roughness of the material. Additionally, the FTIR (Figure 2F) and nano-FTIR spectra (Figure 5A) revealed the introduction of hydrophilic groups, such as -CO and -OH, in the CA CDs and the transition interface layer on the material's surface. These factors collectively enhanced the hydrophilicity of the composite, as evidenced by water contact angle measurements (Figure 6K), which decreased from 71.79 ± 2.17° for pure PTMPTA to 51.93 ± 3.93° for 10%CA CDs/PTMPTA composites. Furthermore, the presence of CA CDs and the transition interface layer contributed to an increase in the material's Young's modulus, which further supported bone cell growth. These combined enhancements promoted improved cell adhesion and proliferation. Additionally, CDs were associated with lower toxicity and were less likely to induce adverse biological reactions [19]. On the 10% CA CDs/PTMPTA composite samples, although cells grew normally in some areas of the composite surface, in other areas no cells survived (Figure 6J). A possible reason for this is that the high proportion of CA CDs in the composites may shield the PTMPTA matrix from UV irradiation, thereby impairing complete photopolymerization and resulting in residual uncrosslinked monomers. Simultaneously, too much CA CDs can accelerate the degradation of the composite, potentially lead to the release of unreacted or degraded monomers. These monomers can locally accumulate and exert cytotoxic effects, thereby impairing cell attachment and proliferation. To directly verify this hypothesis, we conducted FTIR analysis on the culture medium from the cell viability assay (Figure S12). The results revealed a pronounced TMPTA monomer signal in the medium of the 10% CA CDs/PTMPTA group, while no significant monomer release was detected in groups with lower CA CDs content. This together with the highest cell viability observed on the 8% CA CDs/PTMPTA composite shows that 8 wt% CA CDs represents the maximum action concentration that can achieve controlled degradation while maintaining high cell compatibility, making it the optimal formulation for biomedical applications.

CA CDs were also observed to enhance the accuracy of Stereolithography (SLA) 3D printing. Different CA CDs/TMPTA prepolymers were utilized as inks to 3D print woodpile structures, the resolution of all printing process is set as 10 μm and each layer exposed for 0.5s. The designed woodpile structures featured square holes with a side length of 480 μm and microstructure widths of 100 μm ($l \times w$=480 μm × 100 μm) (Figure S9). The printing accuracy improved consistently with increasing CA CDs content up to 8 wt% (Pure PTMPTA was unable to replicate the designed structure accurately, whereas the 8% CA CDs/PTMPTA composite successfully achieved a structure closely resembling the target design (Figures 7A-E). However, similar to the compression test samples, the 3D-printed 10% CA CDs/PTMPTA composites contained an excessive amount of CA CDs agglomerates, resulting in excessive turbidity that hindered curing and ultimately led to scaffold collapse (Figure 7F). The print resolution of all materials is determined by $l \times w$ dimensions and is listed in Table S5. As a result, the structures printed with 8% CA CDs/PTMPTA demonstrated the highest accuracy ($l \times w$=476.3 ± 14.3 μm × 117.4 ± 13.3 μm) (Figure 7E).

The impact of CA CDs on the printing accuracy of PTMPTA was investigated by considering the intrinsic properties of both TMPTA and CA CDs. TMPTA, which contains three acrylic functional groups, exhibited a very rapid curing rate [6]. Consequently, if the UV exposure time exceeded the necessary curing duration during printing, excessive UV light would cause the cured resin to extend beyond the intended layer boundary and blur fine details. In addition, the curing process of TMPTA released a considerable amount of heat, leading to warping or shrinkage of the printed parts [41]. In the results obtained with pure PTMPTA, the printed structures appeared fused together,

obscuring fine details (Figure 7A). CA CDs appeared to address these concerns. When CA CDs were dispersed in a TMPTA solution and their absorbance was measured (Figure 7G), results were compared to the absorbance of CA CDs in water, eliminating the effects of TMPTA and water. It was observed that CA CDs exhibited higher absorbance in TMPTA than in water, indicating that CA CDs can effectively absorb UV light in TMPTA and help mitigate excessive curing beyond the intended boundaries. Meanwhile, increasing the concentration of CA CDs did not cause a substantial rise in absorbance. Even with a tenfold increase in concentration (10 g/L, red curve vs. 1 g/L, black curve), their absorbance remained similar (around 0.5 Absorbance Unit (A.U.)), ensuring that UV light absorption did not significantly hinder the photocuring process. Furthermore, based on the s-SNOM observations of the transition interface layer between PTMPTA and CA CDs (Figure 5D), the heat generated during TMPTA curing could be conducted through this interface. The transition interface layer also adapted to the disparate thermal expansion coefficients of PTMPTA and CA CDs, thereby reducing potential thermal stress arising from temperature fluctuations [43]. This minimized warping and shrinkage, ultimately enhancing the precision of the printed constructs. A time-dependent curing depth experiment (Figure S10) confirmed that increasing CA CDs content progressively declined the curing depth and rate, consistent with their role as light absorbers moderating polymerization kinetics. Photo-DSC analysis (Figure S11) further demonstrated that CA CDs reduced the exothermic peak during photopolymerization, corroborating their function in thermal regulation and stress mitigation. Collectively, these effects enabled precise control over curing dynamics. The 8 wt% CA CDs/PTMPTA formulation exhibited the optimal balance of curing efficiency, dimensional fidelity, and stress reduction. The 8% CA CDs/PTMPTA prepolymer ink was then successfully used to fabricate two types of complex structures: a gyroid structure and a lattice structure (Figure S12) [44], [45]. Both designs were printed with high precision at different sizes (The large structure has a side length of 2.5 cm and the small structure has a side length of 0.8 cm), achieving the intended intricate geometries (Figure 7H-I) (The resolution is set as 40 μm for larger printing size, and 10 μm for smaller size). These results demonstrate that 8% CA CDs/PTMPTA prepolymer ink is highly suitable for high-precision 3D printing and holds significant potential for applications in bone tissue engineering (BTE) [46], [47], [48], [49].

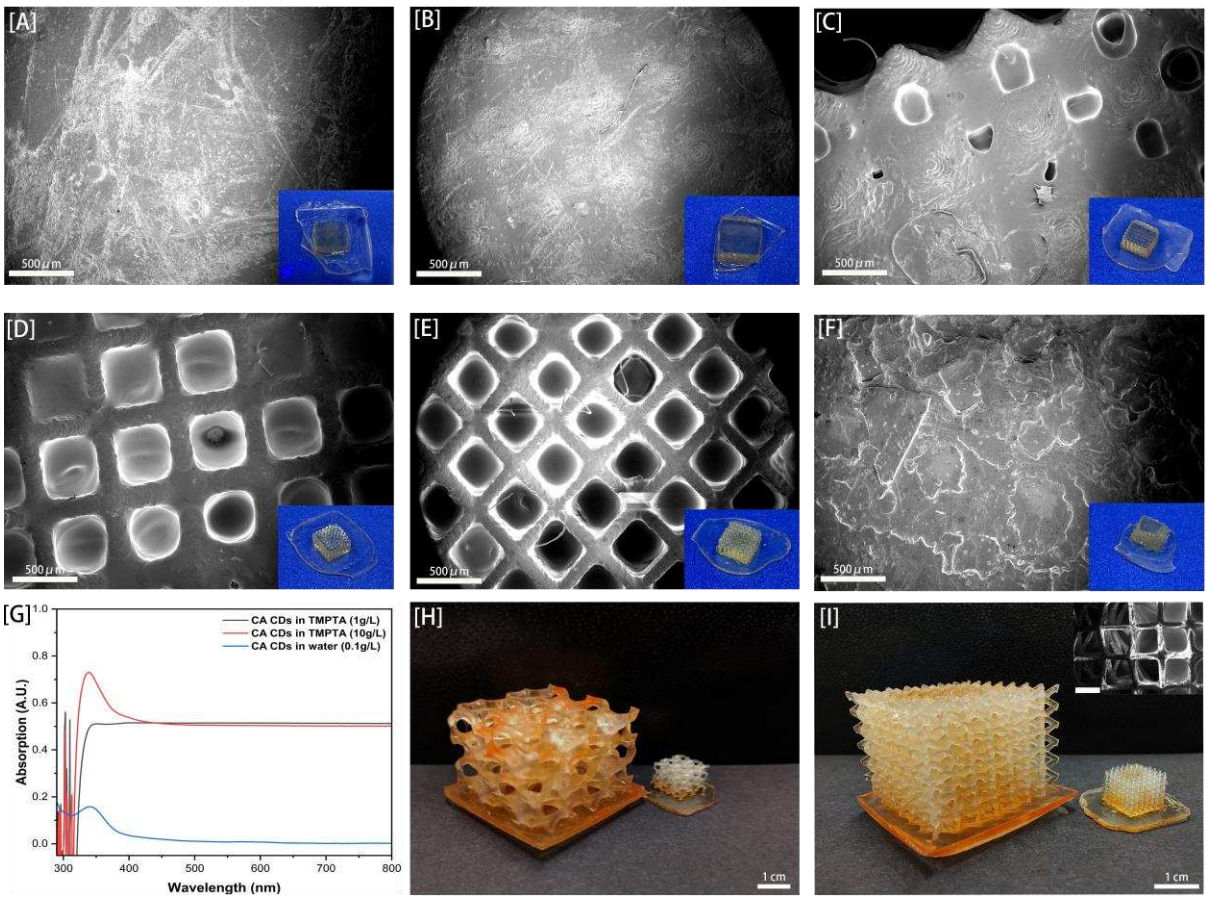

Figure 7. (A-F): The SEM images of 3D-printed scaffolds of pure TMPTA polymer and CA CDs/TMPTA composites, and the inset image in the lower right corner of each image is the 3D-printed scaffold. (G): The absorption spectrum of CA CDs in TMPTA prepolymer (1 g/L (black curve) and 10 g/L（red curve） in TMPTA prepolymer) compared with the absorption spectrum of CA CDs in deionized water (0.1 g/L (blue curve)). (H) Two 3D-printed gyroid scaffold fabricated with varying precision levels: the larger scaffolds had a printing accuracy of 50 microns, while the smaller scaffolds achieved a finer accuracy of 10 microns. (I) Two 3D-printed lattice structure scaffolds fabricated with varying precision levels: the larger scaffolds had a printing accuracy of 50 microns, while the smaller scaffolds achieved a finer accuracy of 10 microns. Inset image is the SEM images of the smaller scaffold. Scale bar of all SEM figures is 500 microns and of all scaffold pictures in Figure H and I is 1 cm.

3. Conclusion

In this study, CA CDs were successfully blended into PTMPTA to form a novel composite material that enhanced the mechanical properties, biocompatibility, and 3D printing accuracy of PTMPTA. Specifically, the 8 wt% CA CDs/PTMPTA composites demonstrated the best overall performance. The tensile Young's modulus of the 8 wt% CA CDs/PTMPTA composite was 1.5-fold increase (363.70 ± 11.96 MPa) to that of pure PTMPTA (240.78 ± 28.42 MPa), while the compressive Young's modulus and maximum load-bearing capacity increased by 3.5-fold to 18.70 ± 1.32 kN and 908.68 ± 98.10 MPa. 8 wt% CA CDs/PTMPTA composites exhibited superior cell viability and cell attachment rates compared to all other weight percentage composites indicating better

biocompatibility (the cell viability increasing almost 2 times compared to that on pure PTMPTA). Furthermore, the 8 wt% composition achieved the highest 3D printing accuracy (Pure PTMPTA failed to replicate the design, while the 8% CA CDs/PTMPTA composite closely matched the target structure). For the first time, via nano-scale spectroscopy and atomic force microscopy techniques it was possible to visually observe the interactions of CA CDs with PTMPTA forming a transitional interface layer, which demonstrated a different chemical structure to pure PTMPTA and pure CA CDs. All improvements to the novel composite could be attributed to the presence of the transition interface layer. This interface layer might ensure more uniform stress distribution, mitigate stress concentration, and strengthen the bonding between CA CDs and the PTMPTA matrix. Furthermore, the interface layer could alter the crystallinity of the material, facilitating better load transfer. The interface layer may play a critical role in preventing voids or defects resulting from the agglomeration of CA CDs. The layer also could inhibit the sliding or separation of aggregates under pressure, thereby reducing the likelihood of premature failure under load. Combined with the inherently high modulus of CA CDs (more than 1 GPa according to DMT Modulus in AFM test), these factors collectively contributed to the significant improvement in the mechanical properties of PTMPTA. The transition interface layer may also enhance heat dissipation during PTMPTA curing and accommodate the different thermal expansion coefficients of PTMPTA and CA CDs, thereby reducing potential thermal stress and improving printing accuracy. Moreover, the UV absorbance strength of CA CDs in the PTMPTA solution helped mitigate over-curing without significantly hindering the photocuring process. The 8 wt% CA CDs/PTMPTA composite demonstrated the capability to produce high-precision scaffolds through SLA 3D printing. Simultaneously, the incorporation of surface roughness and hydrophilic groups through CA CDs and the transition interface layer enhanced the surface hydrophilicity of the material (The water contact angle of the 10% CA CDs/PTMPTA composite is reduced by nearly 20° compared to PTMPTA). In addition, the presence of CA CDs and transition interface layer also accelerated the degradation of the composites, indicating their potential bioabsorbability. Combined with the improved mechanical strength, these factors collectively promoted bone cell adhesion and proliferation, thereby significantly enhancing the material's overall biocompatibility. Nevertheless, the inherent limitations of PTMPTA could not be fully eliminated by CA CDs, there is still room for further enhancement to match the mechanical performance of Weight-Bearing Bones. However, the insights presented in this study – most notably the formation of a transition interface layer – could similarly arise in other carbon dot/polymer systems, making the systems promising for future artificial scaffolds.

4 Experimental Section

Materials

Critic acid, ethyl acetate, diphenyl (2,4,6-trimethyl benzoyl)-phosphine oxide (photoinitiator), ethanol, methanol, toluene, 1 M NaOH, phosphate buffer solution (PBS), Dulbecco's modified eagle's medium (DMEM), L-glutamine, amphotericin B, foetal bovine serum (FBS), penicillin/streptomycin (P/S), trypsin, MG63 cells were all purchased from Sigma-Aldrich

(Darmstadt, Germany). Trimethylolpropane triacrylate (TMPTA), Spectra/Por®7 1kD dialysis membrane and 1M HCL, Calcein Green AM, ethidium bromide, MEM non-essential amino acids (NEAA) are purchased from Thermo Fisher Scientific Inc. (Waltham, MA, USA) and deionized (DI) water.

Preparation of citric acid CDs (CA CDs)

Citric acids were directly heated and carbonized in microwave (CEM Discover® 2.0 (CEM Corporation, Matthews, NC, USA)) at 180°C for 5 minutes. Then the liquid mixture was centrifuged to remove insoluble impurities after cooling down (Thermo Fisher Scientific, Waltham, MA, USA). The yellow supernatant was collected, added with 1 M NaOH and then neutralized with 1 M HCl. The neutralized solution was dialysed 24 hours in DI water by a dialysis bag with pore size up to the penetration of 1 kDa molecular weight. Purified dark brown powdery CA CDs were acquired from the lyophilization (Labogene Scanvac CoolSafe Basic Freeze Dryer (LaboGene™, Lillerød, Danmark)) and vacuum drying (Fistreem Vacuum Oven (Fistreem International Ltd, Cambridge, UK) of the dialysed solution.

Preparation of pure PTMPTA polymer and CA CDs /PTMPTA composites

The purified CA CDs were mixed with liquidous TMPTA, with mass ratios of CA CDs to TMPTA selected at 2%, 4%, 6%, 8%, and 10%. Each mixture was dispersed in ethyl acetate until fully dispersed, then placed in vacuum (Fistreem Vacuum Oven, Fistreem International Ltd, Cambridge, UK) until the ethyl acetate was completely evaporated, and the left-over liquids were CA CDs/TMPTA prepolymer solutions. The solutions were added with 2% photoinitiators and irradiated under 365nm UV light (Dymax BlueWave® FX-1250 High Intensity LED UV Curing Flood Lamp (Dymax®, Wiesbaden, Germany)) for 90s to produce photocured CDs/PTMPTA composites of CDs at 2 ,4, 6, 8, 10 wt% respectively.

Preparation of 3D-printed PTMPTA and CA CDs /PTMPTA composites

For 3D printing, scaffold structures were fabricated using the Micro-15 3D Printer (MicroSLA, Dublin, CA, USA) for small-scale structures and the Mars 3 Pro 3D Printer (ELEGOO, Shenzhen, China) for larger-scale structures, with CA CDs/TMPTA prepolymer solutions utilized as the printing inks. The resolution is set as 40 μm for larger printing size, and 10 μm for smaller size, each layer exposed for 0.5s. The self-designed woodpile structures featured square holes with a side length of 480 μm and microstructure widths of 100 μm (l × w=480 μm × 100 μm) (Figure S9), while the cubic vertex centroid lattice structure (referred to as the "lattice structure") and the gyroid structure were sourced from Thingiverse.com [44], [45] (Figure S10). Modifications to these designs were made using Autodesk Fusion 360.

Characterizations

TEM images, SEM images, and particle size distribution of CA CDs were analysed using JEOL F200 TEM (JEOL Ltd., Tokyo, Japan), FEI Helios Nanolab G3 with Quorum PP3010T cryo-SEM preparation system (Field Electron and Ion Company, Hillsboro, OR, USA) and Zetasizer Nano ZS90 Size Analyzer (Malvern Panalytical Ltd., Malvern, UK), respectively. Absorption and emission spectra of CA CDs were measured with Varian Cary 50 UV-vis Spectrometer (Agilent, Santa Clara, CA, USA) and Horiba FluoroMax-4 Spectrofluorometer (HORIBA, Ltd., Kyoto, Japan). XRD analysis was performed using Panalytical Aeris X-ray Diffraction Spectroscopy (Malvern Panalytical Ltd., Malvern, UK). FTIR spectra were recorded on PerkinElmer Frontier Fourier Transform Infrared Spectrometer (PerkinElmer, Waltham, MA, USA). XPS spectra were acquired with Axis Ultra spectrometer using Al Kα X-rays. Tensile tests of PTMPTA and CA CDs/PTMPTA composites were conducted using MultiTest-dV tester (Mecmesin, Slinfold, UK) with samples laser-cut into dog-bone shapes (1 mm × 2 mm working area) using Laserscript LS3040 (Trotec Laser GmbH, Boldon, UK). Compression tests were performed on Zwick Röell AllroundLine Z050 (ZwickRoell Ltd., Worcester, UK) using cylindrical samples of around 9.5 mm diameter and 4 mm height, those machines can directly test the area of samples working areas. Crosslink density was analyzed by NMR using a Bruker AVIIIHD 400 NMR spectrometer (Blue Scientific Limited, Cambridge, UK). The surface morphology of 8% CA CDs/PTMPTA was measured using a Bruker Dimension Icon AFM (Bruker, Santa Barbara, CA), and Nano-FTIR and s-SNOM were performed using a nanoSCOPE instrument from attocube systems AG (please see SI for more details). Cell viability tests were conducted on MG63 osteoblasts (P9-P17) cultured on PTMPTA and CA CDs/PTMPTA composites, using a microplate reader (FLX800, BIO-TEK Instruments, Inc., Agilent, Santa Clara, CA, USA) with excitation and emission wavelengths of 540 nm and 630 nm, respectively. Live/dead imaging of cells was performed under a Nikon A1 Confocal microscope (Nikon Corporation, Tokyo, Japan). Kruss DSA100 Optical Contact Angle Meter (KRÜSS, Bristol, UK) was used to measure the water contact angle of PTMPTA and CA CDs/PTMPTA composites.

Further details of the characterization methods can be found in the supporting information.

Acknowledgements

The authors acknowledge the financial assistance provided to Woming Gao, Zeming Cheng and David A. Gregory by the University of Sheffield. The authors would like to thank the Engineering and Physical Sciences Research Council (EPSRC) for funding EP/V012126/1 to Cornelia Rodenburg and Nicholas T.H Farr. Frederik Claeyssens also thanks the Royal Society for funding a Royal Society Leverhulme Trust Senior Research Fellowship 2022 (SRF\R1\221053). Alexander J. Knight and Alexander I. Tartakovskii also acknowledge support from the EPSRC grant EP/V007696/1. Confocal imaging work was performed at the Wolfson Optical Microscopy Facility, and TEM (with thanks to Jiahui Qi) and SEM work was performed at Sorby Centre for Electron Microscopy. We thank Dean Haylock for providing the Zwick Röell AllroundLine Z050 and TestResources Hounsfield Universal Test Machine mechanical strength testing equipment. We thank Khalid Doudin for helping with measuring the NMR data. We also wish to acknowledge the

support of the Henry Royce Institute for XPS test at University of Manchester.

Conflict of Interest

The authors declare no conflict of interest.

Reference

[1] Y. Niu, T. Du, and Y. Liu, ‘Biomechanical Characteristics and Analysis Approaches of Bone and Bone Substitute Materials’, *J. Funct. Biomater.*, vol. 14, no. 4, pp. 212, Apr. 2023, doi: 10.3390/jfb14040212.

[2] B. Wingender, P. Bradley, N. Saxena, J. W. Ruberti, and L. Gower, ‘Biomimetic organization of collagen matrices to template bone-like microstructures’, *Matrix Biol.*, vol. 52–54, pp. 384–396, May 2016, doi: 10.1016/j.matbio.2016.02.004.

[3] A. Kumar, K. C. Nune, L. E. Murr, and R. D. K. Misra, ‘Biocompatibility and mechanical behaviour of three-dimensional scaffolds for biomedical devices: process–structure–property paradigm’, *Int. Mater. Rev.*, vol. 61, no. 1, pp. 20–45, Jan. 2016, doi: 10.1080/09506608.2015.1128310.

[4] A. J. Engler, S. Sen, H. L. Sweeney, and D. E. Discher, ‘Matrix Elasticity Directs Stem Cell Lineage Specification’, *Cell*, vol. 126, no. 4, pp. 677–689, Aug. 2006, doi: 10.1016/j.cell.2006.06.044.

[5] K. M. Percival, V. Paul, and G. A. Husseini, 'Recent Advancements in Bone Tissue Engineering: Integrating Smart Scaffold Technologies and Bio-Responsive Systems for Enhanced Regeneration’, *Int. J. Mol. Sci.*, vol. 25, no. 11, pp. 6012, Jan. 2024, doi: 10.3390/ijms25116012.

[6] D. Kirkland and P. Fowler, ‘A review of the genotoxicity of trimethylolpropane triacrylate (TMPTA)’, *Mutat. Res. Toxicol. Environ. Mutagen.*, vol. 828, pp. 36–45, Apr. 2018, doi: 10.1016/j.mrgentox.2018.02.006.

[7] X. Z. Kong, X. L. Gu, X. Zhu, and L. Zhang, ‘Precipitation Polymerization in Ethanol and Ethanol/Water to Prepare Uniform Microspheres of Poly(TMPTA-styrene)’, *Macromol. Rapid Commun.*, vol. 30, no. 11, pp. 909–914, Jun. 2009, doi: 10.1002/marc.200800772.

[8] B. Zhao, J. Li, Y. Xiu, X. Pan, Z. Zhang, and J. Zhu, ‘Xanthate-Based Photoiniferter RAFT Polymerization toward Oxygen-Tolerant and Rapid Living 3D Printing’, *Macromolecules*, vol. 55, no. 5, pp. 1620–1628, Mar. 2022, doi: 10.1021/acs.macromol.1c02521.

[9] Z. Yan *et al.*, ‘Strengthening waterborne acrylic resin modified with trimethylolpropane triacrylate and compositing with carbon nanotubes for enhanced anticorrosion’, *Adv. Compos. Hybrid Mater.*, vol. 5, no. 3, pp. 2116–2130, Sep. 2022, doi: 10.1007/s42114-022-00554-8.

[10] M. Guvendiren, B. Purcell, and J. A. Burdick, ‘9.22 - Photopolymerizable Systems’, in *Polymer Science: A Comprehensive Reference*, K. Matyjaszewski and M. Möller, Eds., Amsterdam, Netherlands: Elsevier, 2012, pp. 413–438. doi: 10.1016/B978-0-444-53349-4.00227-2.

[11] H.-S. Kim and H.-J. Kim. "Enhanced hydrolysis resistance of biodegradable polymers and bio-composites." *Polym. Degrad. and Stab.,* vol. 93, no. 8, pp. 1544–1553, Aug. 2008, doi:

10.1016/j.polymdegradstab.
[12] P. Ammann and R. Rizzoli, ‘Bone strength and its determinants’, *Osteoporos. Int.*, vol. 14, no. 3, pp. 13–18, Mar. 2003, doi: 10.1007/s00198-002-1345-4.
[13] C. Chen *et al.*, ‘In Vitro and In Vivo Characterization of Pentaerythritol Triacrylate-co-Trimethylolpropane Nanocomposite Scaffolds as Potential Bone Augments and Grafts’, *Tissue Eng. Part A*, vol. 21, no. 1–2, pp. 320–331, Jan. 2015, doi: 10.1089/ten.tea.2014.0018.
[14] H. Chen, B. Chen, J. Li, H. Yan, Y. Zeng, and J. Chen, ‘Optimization of Vat-Polymerization binder formulation for 3D printing ceramic slurry using D-optimal mixture experimental design’, *Compos. Part B Eng.*, vol. 260, pp. 110777, Jul. 2023, doi: 10.1016/j.compositesb.2023.110777.
[15] X. Xu *et al.*, ‘Electrophoretic Analysis and Purification of Fluorescent Single-Walled Carbon Nanotube Fragments’, *J. Am. Chem. Soc.*, vol. 126, no. 40, pp. 12736–12737, Oct. 2004, doi: 10.1021/ja040082h.
[16] K. Chang, Q. Zhu, L. Qi, M. Guo, W. Gao, and Q. Gao, ‘Synthesis and Properties of Nitrogen-Doped Carbon Quantum Dots Using Lactic Acid as Carbon Source’, *Materials*, vol. 15, no. 2, pp. 466, Jan. 2022, doi: 10.3390/ma15020466.
[17] D. Krok *et al.*, 'Highly efficient carbon dot-based photoinitiating systems for 3D-VAT printing’, *Polym. Chem.,* vol. 14, no. 38, pp. 4429–4444, Sept. 2023, DOI: 10.1039/d3py00726j.
[18] S. Ganguly, P. Das, M. Bose, S. Mondal, A. K. Das, and N. C. Das, ‘Strongly blue-luminescent N-doped carbogenic dots as a tracer metal sensing probe in aqueous medium and its potential activity towards *in situ* Ag-nanoparticle synthesis’, *Sens. Actuators B Chem.*, vol. 252, pp. 735–746, Nov. 2017, doi: 10.1016/j.snb.2017.06.068.
[19] S. Gogoi, M. Kumar, B. B. Mandal, and N. Karak, ‘A renewable resource based carbon dot decorated hydroxyapatite nanohybrid and its fabrication with waterborne hyperbranched polyurethane for bone tissue engineering’, RSC Adv., vol. 6, no. 31, pp. 26066-26076, Apr. 2016, doi.org/10.1039/C6RA0234J.
[20] L. Qiao *et al.*, ‘Ultrafast Visible-Light-Induced ATRP in Aqueous Media with Carbon Quantum Dots as the Catalyst and Its Application for 3D Printing’, *J. Am. Chem. Soc.*, vol. 144, no. 22, pp. 9817–9826, Jun. 2022, doi: 10.1021/jacs.2c02303.
[21] H. Poerwono *et al.*, ‘Citric Acid’, in *Analytical Profiles of Drug Substances and Excipients*, vol. 28, H. G. Brittain, Ed., San Diego, California: Academic Press, 2001, pp. 1–76. doi: 10.1016/S1075-6280(01)28002-1.
[22] J. Guo *et al.*, ‘Yellow-Emissive Carbon Dots with High Solid-State Photoluminescence’, *Adv. Funct. Mater.*, vol. 32, no. 20, pp. 2110393, May. 2022, doi: 10.1002/adfm.202110393.
[23] B. Wang *et al.*, ‘Rational Design of Multi-Color-Emissive Carbon Dots in a Single Reaction System by Hydrothermal’, *Adv. Sci.*, vol. 8, no. 1, pp. 2001453, Jan. 2021, doi: 10.1002/advs.202001453.
[24] W. Li et al., "Carbon-quantum-dots-loaded ruthenium nanoparticles as an efficient electrocatalyst for hydrogen production in alkaline media." *Adv. Mat.* vol. 30, no. 31, pp. 1800676, Aug. 2018, doi: 10.1002/adma.201800676.
[25] H. Ding, S.-B. Yu, J.-S. Wei, and H.-M. Xiong, ‘Full-Color Light-Emitting Carbon Dots with a Surface-State-Controlled Luminescence Mechanism’, *ACS Nano*, vol. 10, no. 1, pp. 484–491, Jan. 2016, doi: 10.1021/acsnano.5b05406.
[26] S. Lu *et al.*, ‘Near-Infrared Photoluminescent Polymer–Carbon Nanodots with Two-Photon

Fluorescence', *Adv. Mater.*, vol. 29, no. 15, pp. 1603443, Apr. 2017, doi: 10.1002/adma.201603443.
[27] M. Igisu *et al.*, 'Changes of aliphatic C–H bonds in cyanobacteria during experimental thermal maturation in the presence or absence of silica as evaluated by FTIR microspectroscopy', *Geobiology*, vol. 16, no. 4, pp. 412–428, Jul. 2018, doi: 10.1111/gbi.12294.
[28] B. Sun, S. Li, X. Jiang, X. Zhu, and X. Z. Kong, 'Synthesis of post-modified poly(ester-amino) microspheres via aza-Michael precipitation polymerization and its use for enzyme immobilization', *Polym. Adv. Technol.*, vol. 32, no. 4, pp. 1802–1812, Apr. 2021, doi: 10.1002/pat.5221.
[29] F. Dai, Q. Zhuang, G. Huang, H. Deng, and X. Zhang, 'Infrared Spectrum Characteristics and Quantification of OH Groups in Coal', *ACS Omega*, vol. 8, no. 19, pp. 17064–17076, May 2023, doi: 10.1021/acsomega.3c01336.
[30] I. Y. Miranda-Valdez *et al.*, 'Bio-Based Foams to Function as Future Plastic Substitutes by Biomimicry: Inducing Hydrophobicity with Lignin', *Adv. Eng. Mater.*, vol. 26, no. 20, pp. 2400233, Oct. 2024, doi: 10.1002/adem.202400233.
[31] F. Bauer, U. Decker, S. Naumov, and C. Riedel, 'Photoinitiator-free UV curing and matting of acrylate-based nanocomposite coatings: Part 3', *Prog. Org. Coat.*, vol. 77, no. 6, pp. 1085–1094, Jun. 2014, doi: 10.1016/j.porgcoat.2014.03.013.
[32] Q. Shen, Y. Zhang, Y. Fan, Z. Xu, and Z.-X. Sun, 'Adsorption behavior of heptyl xanthate on surface of ZnO and Cu(II) activated ZnO using continuous online in situ ATR-FTIR technology', *Trans. Nonferrous Met. Soc. China*, vol. 32, no. 7, pp. 2370–2378, Jul. 2022, doi: 10.1016/S1003-6326(22)65953-3.
[33] I. M. Hasanah, M. Martosudiro, L. Q. Aini, K. R. Prillianti, and M. R. Prabowo, 'Fourier Transform Infrared (FTIR) Spectroscopy Method for Fusarium solani Characterization', *Res. J. Life Sci.*, vol. 9, no. 1, pp. 22–28, Apr. 2022, doi: 10.21776/ub.rjls.2022.009.01.3.
[34] M. Yu *et al.*, 'Nucleation and crystallization of poly(L-lactide) assisted by terminal hydrogen-bonding segments', *Polymer*, vol. 254, pp. 125031, Jul. 2022, doi: 10.1016/j.polymer.2022.125031.
[35] Y. K. Chae, W. Y. Kang, J.-H. Jang, and S.-S. Choi, 'A simple NMR method to measure crosslink density of natural rubber composite', *Polym. Test.*, vol. 29, no. 8, pp. 953–957, Dec. 2010, doi: 10.1016/j.polymertesting.2010.08.003.
[36] H. Quan, Z.-M. Li, M.-B. Yang, and R. Huang, 'On transcrystallinity in semi-crystalline polymer composites', *Compos. Sci. Technol.*, vol. 65, no. 7, pp. 999–1021, Jun. 2005, doi: 10.1016/j.compscitech.2004.11.015.
[37] T. Li, G. Yu, W. Huang, Y. Chen, Y. Zhu, and C. Liang, 'Influence of multi gradient modulus interface layer constructed by flexible PI nanolayer modified carbon fiber surface on the mechanical properties of epoxy based composites', *J. Mater. Res. Technol.*, vol. 34, pp. 1482–1494, Jan. 2025, doi: 10.1016/j.jmrt.2024.12.176.
[38] B. Song *et al.*, 'Layer-by-layer constructing interface with rigid-flexible transition structure for improving interfacial adhesion of PBO fiber composites', *Compos. Commun.*, vol. 22, pp. 100466, Dec. 2020, doi: 10.1016/j.coco.2020.100466.
[39] M. Mehdikhani, L. Gorbatikh, I. Verpoest, and S. V. Lomov, 'Voids in fiber-reinforced polymer composites: A review on their formation, characteristics, and effects on mechanical performance', *J. Compos. Mater.*, vol. 53, no. 12, pp. 1579–1669, May 2019, doi:

10.1177/0021998318772152.
[40] R. Wang, C. Cheng, H. Wang, and D. Wang, ‘Swollen hydrogel nanotechnology: Advanced applications of the rudimentary swelling properties of hydrogels’, *Chem. Phys. Mater.*, vol. 3, no. 4, pp. 357–375, Oct. 2024, doi: 10.1016/j.chphma.2024.07.006.
[41] F. K. Metze, S. Sant, Z. Meng, H.-A. Klok, and K. Kaur, ‘Swelling-Activated, Soft Mechanochemistry in Polymer Materials’, *Langmuir*, vol. 39, no. 10, pp. 3546–3557, Mar. 2023, doi: 10.1021/acs.langmuir.2c02801.
[42] H.-Y. Park *et al.*, ‘Photo-cationic polymerizable ceramic slurry for the fabrication of ceramic structures in three-dimensional printing’, *Int. J. Appl. Ceram. Technol.*, vol. 22, no. 2, pp. e14954, Mar./Apr. 2025, doi: 10.1111/ijac.14954.
[43] D. Qin, W. Zhu, F. Hai, C. Wang, J. Cui, and Y. Deng, ‘Enhanced Interface Stability of Multilayer Bi2Te3/Ti/Cu Films after Heat Treatment via the Insertion of a Ti Layer’, *Adv. Mater. Interfaces*, vol. 6, no. 20, pp. 1900682, Oct. 2019, doi: 10.1002/admi.201900682.
[44] Thingiverse.com, ‘Lattice Structures - Mikrostrukturen by RobotMama’, Thingiverse. Accessed: Dec. 02, 2024. [Online]. Available: https://www.thingiverse.com/thing:2788117.
[45] Thingiverse.com, ‘Gyroid-structure by reni’, Thingiverse. Accessed: Dec. 02, 2024. [Online]. Available: https://www.thingiverse.com/thing:2585464.
[46] W. Ma, H. Lu, Y. Xiao, and C. Wu, ‘Advancing organoid development with 3D bioprinting’, *Organoid Res.*, vol. 1, no. 1, pp. 004, Mar. 2025, doi: 10.36922/OR025040004.
[47] S. Song et al., ‘Nerve–bone crosstalk manipulates bone organoid development and bone regeneration: A review and perspectives’, *Organoid Res.*, vol. 1, no. 1, pp. 8294, Mar. 2025, doi: 10.36922/or.8294.
[48] Z. Li et al., 'Design, characterisation, and clinical evaluation of a novel porous Ti-6Al-4V hemipelvic prosthesis based on Voronoi diagram’, *Biomater. Transl.*, vol. 5, no. 3, pp. 314–324, Sep. 2024, doi: 10.12336/biomatertransl.2024.03.007.
[49] H. Chu et al., ‘Harnessing decellularised extracellular matrix microgels into modular bioinks for extrusion-based bioprinting with good printability and high post-printing cell viability’, *Biomater. Transl.*, vol. 4, no. 2, pp. 115–127, Jun. 2023, doi: 10.12336/biomatertransl.2023.02.006.

Support information

Additional Characterization Methods Details

Mechanical test

Tensile testing of PTMPTA and all composites was conducted using a MultiTest-dV universal testing machine (Mecmesin, Slinfold, UK). Prepolymer solutions of PTMPTA and its composites were cast into cylindrical silicone molds (100 mm diameter, 1 mm thickness), and a glass plate was placed on top to ensure a smooth surface post-curing. The samples were fully cured under 365 nm UV light using a Dymax BlueWave® FX-1250 high-intensity LED flood lamp (Dymax®, Wiesbaden, Germany) for 90 seconds. Dog-bone-shaped specimens (working area: 10 mm × 2 mm × 1 mm) were then precision-cut from the cured discs using a laser cutter (Laserscript LS3040, Trotec Laser GmbH., Boldon, UK). All tensile tests were performed using a 250 N load cell at a constant crosshead speed of 1 mm/min. Ten specimens (n = 10) were tested for each sample group.

The compressive properties of PTMPTA and all composites were evaluated using Zwick Roell AllroundLine Z050 system (ZwickRoell Ltd., Worcester, UK) with a 50 kN load cell. All tests were performed at a constant crosshead speed of 1 mm/min. The prepolymer solutions were cast into cylindrical silicone molds (9.5 mm diameter × 4 mm height), with a glass plate placed on top to ensure a flat curing surface. The samples were fully cured under 365 nm UV light using a Dymax BlueWave® FX-1250 high-intensity LED flood lamp for 90 seconds. For each material group, five replicate specimens (n = 5) were tested.

No surface polishing was applied, but the molds and laser cutting produced smooth and uniform surfaces across all specimens. The working area of all samples was averaged from three measurements.

Cross-linking density test

For cross-linking density test, equal-sized rectangular samples of the composites were prepared and immersed in toluene for one day, after which excess solvent was removed by gravity. The samples were then placed into NMR tube and were completely submerged by $CDCl_3$. 400 MHz ^1H nuclear magnetic resonance (NMR) (Burker AVIIIHD 400 NMR spectrometer (Blue Scientific Limited, Cambridge, UK)) was carried out. MestReNova software (MestreLab Research, Santiago de Compostela, Spain) was used to analyze the spectra. The cross-link density was assessed by comparing the chemical shifts of functional groups across different samples.

Swelling test

The composite samples were initially weighed (W_{dry}) and then fully immersed in deionized water, PBS (pH = 7.4), and ethanol and incubated at room temperature (25 °C). The samples were reweighed (W_{wet}) on day 1, 3, 5, 7, and 9 after removing surface liquid with filter paper. The swelling ratio was calculated using Eq. (1).

Swelling Ratio (%) $=[(W_{wet} - W_{dry})]/ W_{dry} \times 100$ (1)

The nano-FTIR, AFM, and s-SNOM test

The nano-FTIR, AFM, and s-SNOM data presented in Figure 5 of the main manuscript were taken using a neaSCOPE s-SNOM setup from attocube systems AG. During the nano-FTIR and s-SNOM measurements, laser light was focused down onto the tip of an AFM cantilever coated in metal (ARROW-EFM cantilevers from NanoWorld, Pt/Ir coating) in order to generate surface excitations in the tip's surface. These surface excitations are comprised of a strong, confined electric field component, which is brought into proximity with the sample during tapping mode AFM operation. This electric field probe interacts with the sample and generates a scattering centre, which then scatters further incoming light into the detection path of the system. By using an interferometer setup, with a clean reference mirror in one arm and the AFM system in the other arm, both the amplitude and phase of the scattered light can be recorded. Demodulating the measured signal at harmonics of the AFM tapping frequency, as well as moving the reference mirror (for nano-FTIR – a clean single movement of the mirror along the direction of the interferometer arm, for s-SNOM – a jittering sinusoidal motion applied to the mirror which adds a known addition to the lock-in frequency), allows for the complete suppression of background signal in the measurement data.

AFM parameters: 79kHz tapping frequency, 60-70nm tapping amplitude. The data is levelled to a plane fit.

Nano-FTIR parameters: The broadband illumination source used was a FemtoFiber dichro midIR from TOPTICA Photonic, with spectrum setting 'C' (output range approximately 900-1900 cm^{-1}). The data demodulated at the second harmonic of tapping frequency is presented. The data was referenced to a clean measurement of a silicon test sample. A moving average of five points was applied to smooth the data.

s-SNOM parameters: The illumination source used was a MIRcat-QT from Daylight Solutions operating at 1115cm^{-1}, and the data demodulated at the third harmonic of tapping frequency is presented. s-SNOM amplitude data is normalised to the maximum recorded value, and s-SNOM phase data is offset by the mean recorded value.

In-vitro degradation test

The procedures adopted for the study were conducted in accordance with the recommendations of ISO 10993-13, Biological Evaluation of Medical Devices Part 13: Identification and Quantification of Degradation Products from Polymeric Medical Devices [1]. Uniformly sized composite discs (160 mg, 15 mm diameter) were prepared and thoroughly rinsed with deionized water to remove residual prepolymer and photoinitiator from the surface. The samples were first characterized by FTIR, then immersed in PBS (simulating physiological conditions) and 3% H_2O_2 solution (simulating oxidative degradation), with a solid-to-liquid ratio of 1 g : 10 ml. Degradation was conducted at 37 °C for 14 days. Following the degradation treatment, the samples were washed with deionized water, transferred to clean collection containers, and placed on a Stuart orbital shaker S1500 (Keison Products, Essex, UK) at 115 RPM for 7 additional days. After the full 21-day treatment period, the samples were removed, air-dried at room temperature, weighed, and

analysed again by FTIR. The triplicate of each sample was measured every time.

Cell culture and seeding on samples

MG63 osteoblasts (P9-P17) were revived from -80°C freezer. The culture media was based on Dulbecco's modified Eagle's medium (DMEM) and was supplemented with 10% v/v FBS, 1% v/v L-glutamine, P/S and NEAA and 4% v/v amphotericin B. The cells were incubated at 37°C, 5% CO_2 and were passaged when their confluency under light microscope reached 70% - 80%. The samples were pre-washed in PBS for 7 days for photo initiator and prepolymer removal and were laser cut into discs (15 mm diameter, 1 mm thickness). The sample discs were sticked at the bottom of 24-well plates with non-cytotoxic glue (KingBritish) and disinfected in 70% ethanol aqua solution and then washed in PBS. The cells' concentration was calculated with haemocytometer before seeding and 1×10^4 cells were seeded on each sample.

Cell viability test

The cell viability on the samples was measured via resazurin reduction assay and seeding on TCP as positive control. The resazurin sodium salt was dissolved in PBS in the concentration of 25 mg/100 ml as the master stock and was diluted 10 times in culture media as reaction solution. The MG63 cells were seeded on the scaffolds and the viability was measured on day 1, day 4 and day 7 by replacing the culture media with reaction solution and incubating in the dark at 37°C for 4 hours. Then 200 µl of the solution in each well was transferred to a 96-well plate and was read at the excitation and emission wavelengths of 540 nm and 630 nm in microplate reader (FLX800, BIO-TEK Instruments, Inc., Agilent, Santa Clara, CA, USA). After day 7, all cell-cultured media was collected for FTIR analysis. The spectra were recorded using a PerkinElmer Frontier Fourier Transform Infrared (FTIR) spectrometer (PerkinElmer, Waltham, MA, USA), with blank culture medium on TCP serving as the background reference.

Live/dead assay

1×10^4 MG63 cells were cultivated on the sample discs for 7 days and the culture media was replaced every other day. The live/dead staining solution was made by dissolving the Calcein Green AM in DMSO and dilute the Calcein Green AM DMSO solution and ethidium bromide in PBS. The staining solution was dropped on the sample surface after removing the culture media and the cells were incubated for 10 minutes at 37°C. Then the live/dead cells were imaged at 10× magnification under Nikon A1 Confocal microscope (Tokyo, Japan).

Time-dependent curing depth experiment

TMPTA and all composite prepolymer solutions were transferred into glass tubes (2 cm in diameter, 10 cm in height). To ensure unidirectional exposure, the tube caps and side walls were wrapped in aluminium foil, leaving only the bottom exposed. UV curing was initiated from the base using a M405L2 UV-mounted LED lamp (Thorlabs Inc., Newton, NJ, USA) with an intensity of 700

mW/cm² at 405 nm. Samples were irradiated for varying durations (1, 2, 5, 10, 20, and 30 seconds). Following each exposure, unreacted monomers were removed, and the cured lengths were measured. For each time point, triplicate measurements were performed and averaged to determine the mean curing depth.

Photo-DSC Measurements

The analysis was conducted using a Pyris Diamond DSC (PerkinElmer, Shelton, CT, USA). A M405L2 UV-mounted LED lamp (Thorlabs Inc., Newton, NJ, USA; 405 nm, 700 mW/cm²) was mounted 1 cm above the open sample chamber. Approximately 5 mg of prepolymer sample—TMPTA and all composite prepolymer solutions—was placed in an aluminium DSC pan. The reference was an empty pan. All measurements were performed at 30°C under a nitrogen atmosphere. The UV light source was controlled via a Thorlabs development controller and triggered after a 1-second temperature equilibration. Samples were irradiated for 10 seconds, and the resulting heat flow was continuously recorded.

Dynamic light scattering (DLS)

A Zetasizer Nano ZS90 Size Analyzer (Malvern Panalytical Ltd, Malvern, UK) was used to analyse the particle size of CA CDs and its aggregation. all composite prepolymer solutions were prepared and measured the particle size from 0.3nm to 10 microns (diameter) using 90 degree scattering optics.

Statistical analysis

Differences between groups were assessed using EXCEL standard deviation analysis (STDEV), Originlab 2023's and GraphPad Prism one-way Analysis of Variance (ANOVA) test (for mechanical test, resazurin and water contact angle test), and the results were plotted as mean ± standard deviation (SD). Significant differences between each experimental group were analyzed. Significant difference was defined as $*p < 0.05$. Highly significant differences were defined as $**p < 0.01$, $***p < 0.001$, and $****p < 0.0001$.

SEM image for 8% CA CDs/PTMPTA composites

Cryo-scanning electron microscopy (Cryo-SEM) was conducted using the Quorum PP3010T cryo-SEM preparation system (Quorum Technologies Ltd., Laughton, East Sussex, UK). Specimens were mounted on a cryo-SEM shuttle, and plunge-frozen in slushed liquid nitrogen. The shuttle was then transferred to a cooled prep stage (-160 °C) before being loaded onto the cryo-stage (-160 °C) housed within the SEM chamber for imaging. An anti-contaminator was also

placed within the chamber at a temperature of -185 °C.

A FEI Helios Nanolab G3 (FEI Company, US) microscope was employed for surface morphology observations of 8% CA CDs/PTMPTA composites. In contrast to common scanning electron microscopy (SEM) analysis practice, samples were not pre-treated with a conductive coating by deposition. An accelerating voltage of 1-2 keV at typical chamber vacuum pressures in the range of 10−6 mbar and a working distance of 4 mm were chosen to avoid sample damage through surface charging. An Everhart-Thornley Detector (ETD) was selected for SEM image.

Additional Experimental and Characterization Details

1. Characterization of CA CDs

Upon microwave irradiation the citric acid solution turns yellow and finally orange during its carbonisation process, which indicates the formation of CA CDs (Figure S1A) [2]. Upon completion of the reaction, the products are dispersed in water and centrifuged, neutralized and dialyzed to remove insoluble particles in water and small molecules. The resulting solution is then dried to obtain CA CDs powder (Figure S1B).

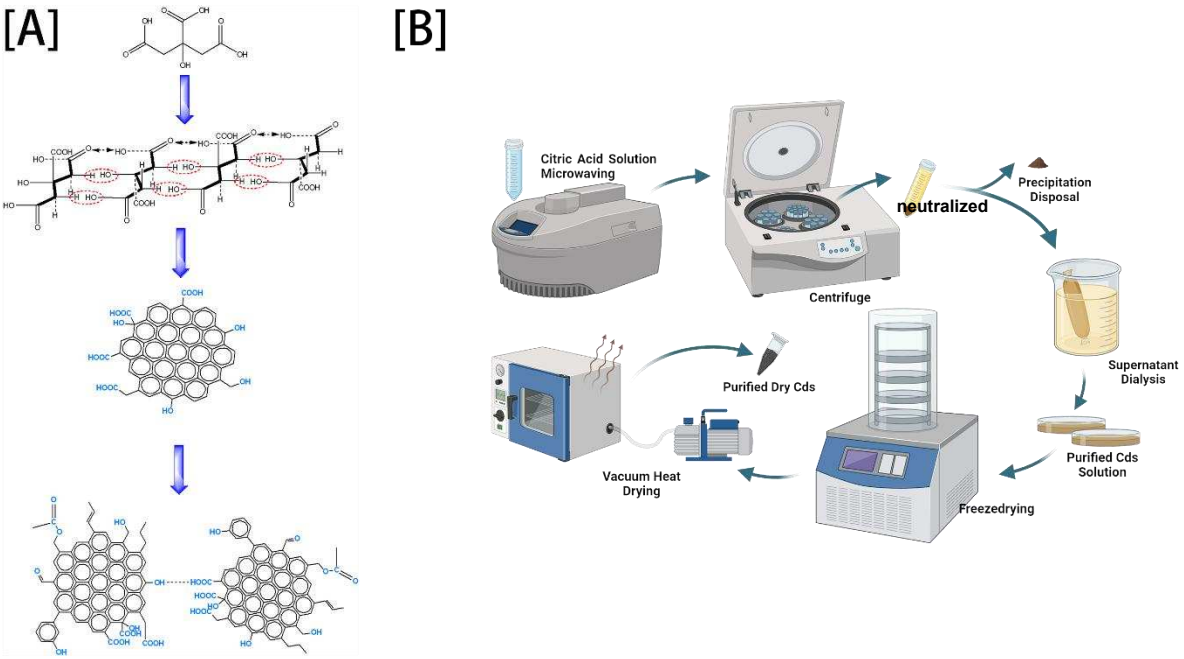

Figure S1. (A) the synthesis of CA CDs; (B) The production process of CA CDs.

We explore the chemical structures of the CA CDs, XRD, FTIR, NMR and XPS characterization of CDs was conducted. In XRD pattern (Figure S2A), the appearance of a broad peak at approximately 20° further indicates the high degree of graphitization within the CD core. This broad peak corresponds to a graphite-like structure, with an interlayer distance of 0.44 nm (002). Compared to the 0.335 nm layer spacing of pure graphite, the increased spacing may be attributed to the steric hindrance of functional groups at the edges of the sp^2-carbon planes or to planar distortion caused by sp^3 carbon within the sp^2-carbon domain [3]. Additionally, a minor peak was observed at $2\theta = 43°$ in the XRD pattern, which corresponds to the (100) plane of graphene with a lattice fringe spacing of 0.21 nm [4].

According to FTIR result (Figure S2B), the peak around 3500 cm^{-1} is attributed to the O-H stretching on hydroxyls and phenols. The peaks in the 3000-3100 cm^{-1} range correspond to the =C-H stretching vibration of aromatic and alkenes, while those around 2850 cm^{-1} are associated with the -C-H stretching vibration of saturated hydrocarbons. The peak at approximately 1688 cm^{-1} can be assigned to C=O on ketones, aldehydes, carboxylic acids, esters or C=C on alkenes. The fingerprint region peaks around 1350-1470 cm^{-1} are indicative of the bending or deformation vibrations of C-H on methyl and methylene groups, and the region between 1000-1350 cm^{-1} corresponds to the C-O stretching vibration on alcohol, phenol, ether and carboxylic acid. Peaks below 1000 cm^{-1} are attributed to -C-H bending vibration in aromatic hydrocarbon substituents. The above results revealed the presence of various functional groups on the CA CDs including hydrocarbons, hydroxyls, carbonyls, esters, and aromatic rings.

For NMR, both ^{1}H and ^{13}C NMR spectroscopy were done to further confirm CA CDs' structures. According to ^{1}H NMR (Figure S2C), the signal around 0.8 ppm (a) corresponds to the methyl hydrogen; The signals around 2.0 ppm (b) can be attributed to CH_2 groups adjacent to a carboxylic group; The signal around 2.8 ppm and 3.0 ppm (c, d) both split into 2 peaks, which can be attributed to protons on CH groups adjacent to hydroxyl, protons on hydroxyl groups and residual citric acid. Signals near 3.37 ppm (e) are assigned to CH_2 protons connected to ester or ether groups; The signals between 5.5 to 7 ppm (g, h) correspond to aromatic or unsaturated CH [5]. Figure S2D presents the ^{13}C NMR spectrum. The signals between 20 and 30 ppm (1) correspond to CH_3 groups; Signals around 40 ppm (2) are attributed to CH_2 carbons adjacent to sp^2-hybridized carbons or oxygen atoms, while those between 60-80 ppm (3) represents quaternary carbon, C-O or C-O carbons. Two signals between 130-140 ppm (4, 5) correspond to sp^2-hybridized carbons (C=C) and C=O on aromatic rings. The peaks between 160-180 ppm (6) are indicative of the C=O on the carboxyl group [6]. The additional peaks observed at 43, 73, 173, and 176 ppm (labelled as CA) are consistent with residual citric acid, as confirmed by the simulation of the ^{13}C NMR spectrum of citric acid (Figure S6). The integration of the peaks in the ^{13}C NMR spectra was subsequently calculated to determine the percentage distribution of carbon atoms in different chemical environments (Figure S7). As presented in Table S1, the content of sp^3 carbon and carbon in C-O groups was determined to be 37.19%, while sp^2 carbon and C=O groups associated with aromatic rings accounted for 40.22%. Additionally, the carboxyl group carbon constituted 22.59% of the total carbon content.

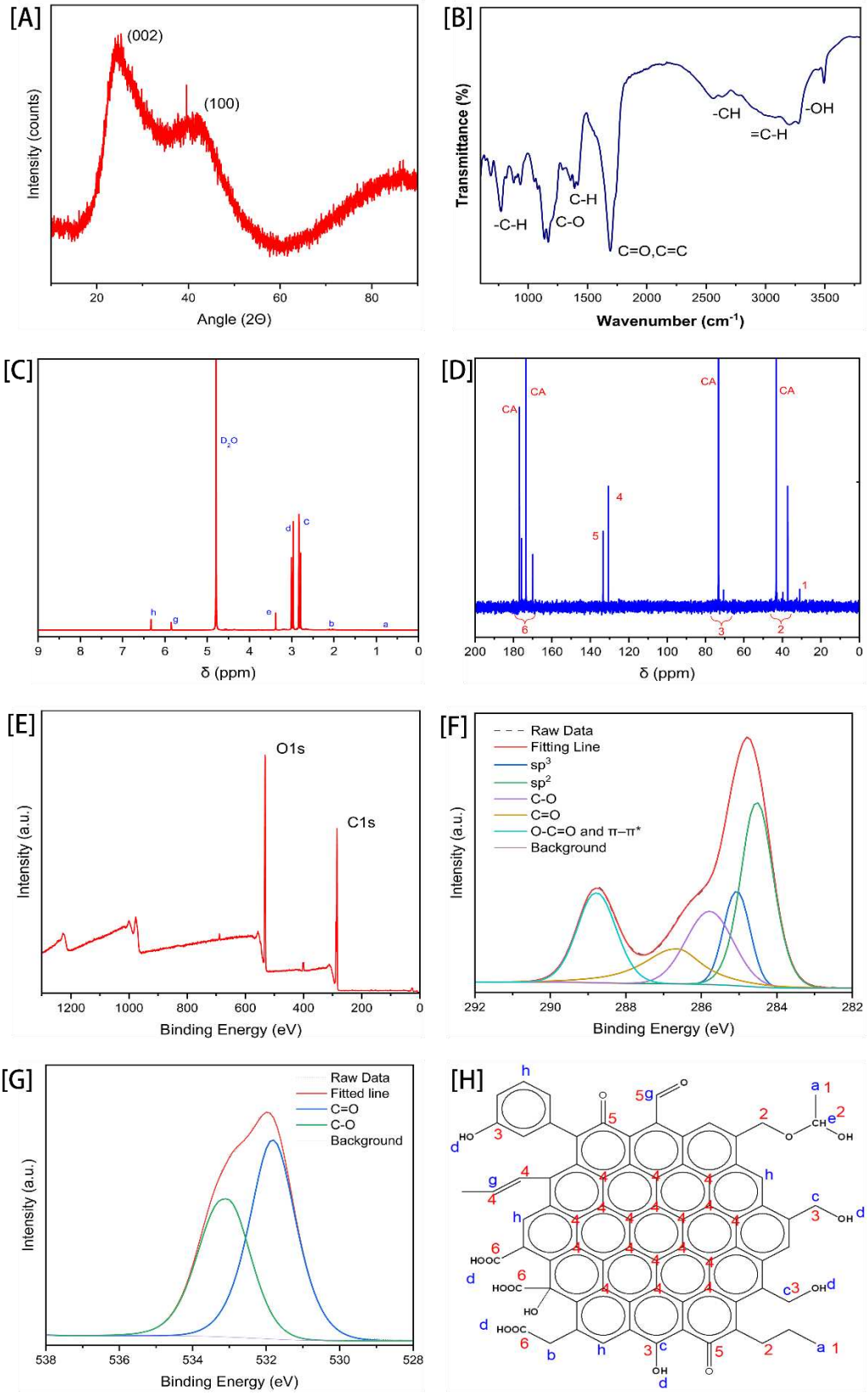

964

965 **Figure S2. Structural characterizations of CA CDs: (A) XRD spectrum; (B) FTIR spectrum; (C) ^{1}H-NMR**
966 **spectrum and (D) ^{13}C-NMR spectrum recorded in D_2O; (E) full XPS survey and high-resolution (F) C 1s and**
967 **(G) O 1s XPS spectra; (H) molecular structure model of CA CDs according to previous spectra.**

Table S1 Comparison of carbon group content measured by ^{13}C NMR and C1s XPS spectrum (Left: 13C NMR; Right: C1s XPS)

^{13}C NMR				C1s XPS			
Signal	Percentage of Signal Area (%)	Carbon group	Content of the group (%)	Peaks	Percentage of Signal Area (%)	Carbon group	Content of group (%)
1	1.99	sp^3 C and C-O	37.19	sp^3	13.71	sp^3 C and C-O	32.77
2	31.23						
3	3.97			C-O	19.06		
4	25.27	C=O on aromatic ring and sp^2 C	40.22	sp^2	34.22	sp2 and C=O	47.53
5	14.95			C=O	13.31		
6	22.59	carboxyl group C	22.59	carboxyl group	19.69	O-C=O	19.69

Figure S2E-G are the XPS patterns, the full survey spectrum (Figure S1E) reveals peaks corresponding to C1s (284.8 eV) and O1s (532.3 eV), indicating that CA CDs primarily consist of carbon and oxygen elements. Trace nitrogen peaks are also detected, which may result from impurities or reactions involving nitrogen in the air during the pyrolysis process; these can be considered negligible. The high-resolution XPS spectrum of C 1s (Figure S1F), after deconvolution, reveals four components: sp^3 C around 284.5 eV, sp^2 (graphitic) C around 285 eV, C-O around 285. 8 eV, and C=O around 287 eV, as well as a carboxyl group and π-π* combined peak around 288.8 eV. Similarly, the O 1s spectrum deconvolution (Figure S1G) identifies two contributions: C-O at 531.8 eV and C=O at 533 eV [6],[7]. Subsequently, the relative composition of each component was quantified based on the area under the C 1s and O1s curve. Analysis of the C 1s spectra (Table S1) revealed that the content of sp^2 carbon was 34.22%, sp^3 carbon was 13.71%, C-O was 19.0%, C=O was 13.31%, and the carboxyl group along with the π-π* contribution accounted for 19.69%. Similarly, the O 1s spectra indicated that the contributions of C-O and C=O oxygen were nearly equivalent, comprising 49.34% and 50.66%, respectively. Table 1 presents a comparison of the carbon group content as measured by ^{13}C NMR and XPS. While some discrepancies in the values are observed, these differences may be attributed to instrumental and calculation errors, as well as the presence of residual citric acid. Nevertheless, the variations are relatively minor.

Based on the above XRD, FTIR, NMR and XPS structural characterization and previous related literature [3], [9], [10], [11], we proposed a molecular structure model of CA CDs (Figure S2H), and CA CDs molecules might underwent π-π stacking interactions, forming integrated structures resembling graphite or pyrolytic carbon [4]. Single CA CDs molecule consisted of at least 19 fused aromatic rings, resulting in a molecular weight that can exceed 1 kDa. This is consistent with the 1 kDa molecular weight cutoff of the dialysis bag used for purification. The core of the CA CD consisted of a polycyclic aromatic hydrocarbon (PAH) structure, with its surface functionalized by various groups.

2. Synthesis of CA CDs /PTMPTA composites

To obtain CA CDs /PTMPTA composites, the purified CA CDs were mixed with the TMPTA prepolymer solution, at the mass ratio of 0%, 2%, 4%, 6%, 8% and 10% to PTMPTA. The mixtures were initially thoroughly dispersed in ethyl acetate (Figure S3A), and then placed in the vacuum until ethyl acetate was fully evaporated, the resulting uniformly mixed CA CDs/PTMPTA prepolymer was subsequently cured under 365nm UV lamp for 90s, forming the final composites (2% CA CDs/PTMPTA composites, 4% CA CDs/PTMPTA composites, 6% CA CDs/PTMPTA composites, 8% CA CDs/PTMPTA composites, and 10% CA CDs/PTMPTA composites). Upon observation, the colour of the prepolymer solution and the cured composites progressively turned more yellow as the concentration of CA CDs increased, suggesting that the CA CDs were successfully integrated into the PTMPTA matrix (Figure S3B and S3C from left to right). When the CA CDs content exceeded 8%, precipitation occurred in the solution, rendering it turbid, and the sample disk becomes opaque, with visible solid aggregates of CA CDs embedded within the composites. This indicates that 8% CA CDs is the maximum concentration that can be uniformly dispersed within the composites.

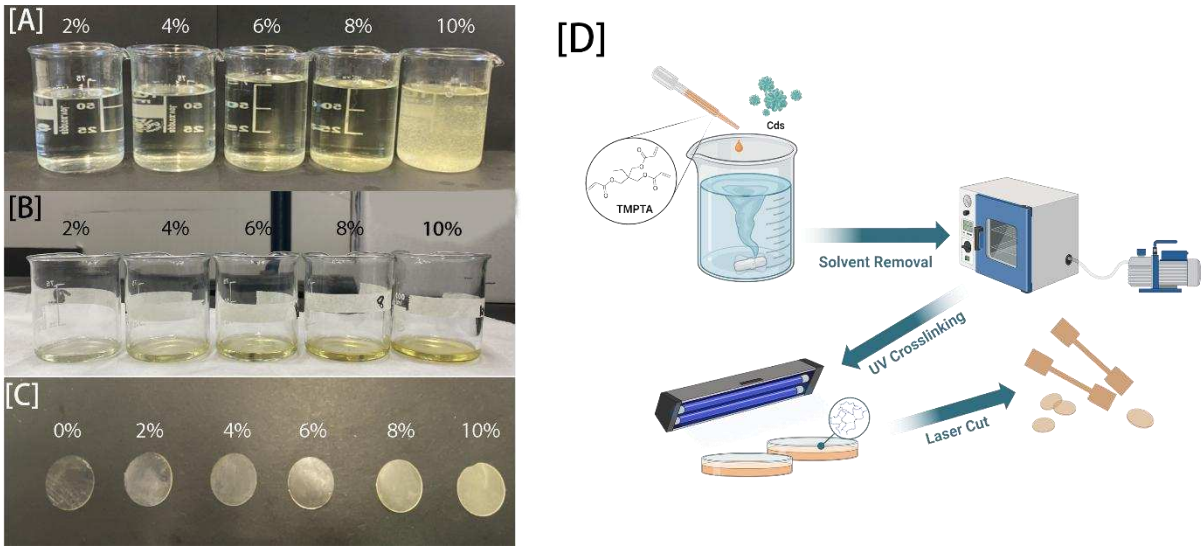

Figure S3. (A) different ratio of CA CDs and TMPTA prepolymer dispersed in ethyl acetate (from left to right: 2% CA CDs, 4% CA CDs, 6% CA CDs, 8% CA CDs, 10% CA CDs and TMPTA in ethyl acetate). (B) the ethyl acetate was removed, and left CA CDs well dispersed in TMPTA prepolymer (from left to right: 2% CA CDs, 4% CA CDs, 6% CA CDs, 8% CA CDs, 10% CA CDs and TMPTA). (C) PTMPTA and CA CDs/PTMPTA composites were made after photocuring (from left to right: PTMPTA, 2% CA CDs /PTMPTA composites, 4% CA CDs /PTMPTA composites, 6% CA CDs /PTMPTA composites, 8% CA CDs /PTMPTA composites, 10% CA CDs /PTMPTA composites). (D) The process flow of making CA CDs/PTMPTA composites.

3. Characterization of swell ratio of CA CDs /PTMPTA composites

The swelling behaviour of the scaffolds is also a crucial indicator for in vivo grafts. The swelling rate significantly impacts the overall performance and efficacy of the scaffolds [12]. Figure S4A-C illustrates the swelling rate of materials over time when immersed in ethanol, deionized water (DI) and PBS respectively. The data indicate that the swelling rate increases with time, reaching a maximum and stabilizing on the 7th day. Generally, the swelling rate of materials is inversely related to their crosslinking density; that is, a higher the swelling rate indicates a lower crosslinking

density [13]. Consequently, we compared the swelling rate with the cross-linking density, revealed that 2% CA CDs/PTMPTA composites, which exhibit the highest cross-linking density, also demonstrate the lowest swelling rate. Conversely, the 10% CA CDs/PTMPTA composites, characterized by the lowest cross-linking density, show the highest swelling rate. However, although the cross-linking density of 4% and 6% CA CDs/PTMPTA composites is higher than that of PTMPTA, the observed swelling rates are contrary to expectations. This anomaly may be attributed to the aggregation of CA CDs within the polymer matrix and their contribution to the overall hydrophilicity of the composites, which facilitates liquid ingress and consequently enhances swelling [14]. Water contact angle measurements (Figure 6K) confirmed an increase in hydrophilicity with increasing CA CDs content. In addition, SEM images of the composites (Figure S13) revealed pronounced aggregation of CA CDs on the surface, with higher CD content leading to more extensive and larger clustering. Compared to all the materials tested in various liquid (Figure S4D), the highest swelling rate observed is approximately 21.5% for the 10% CA CDs/PTMPTA composites in ethanol. In PBS, the maximum swelling rate for the 10% CA CDs/PTMPTA composites is around 14%, with other materials exhibiting swelling rates of 10% or lower. These results indicate that all composites possess relatively low swelling properties [15].

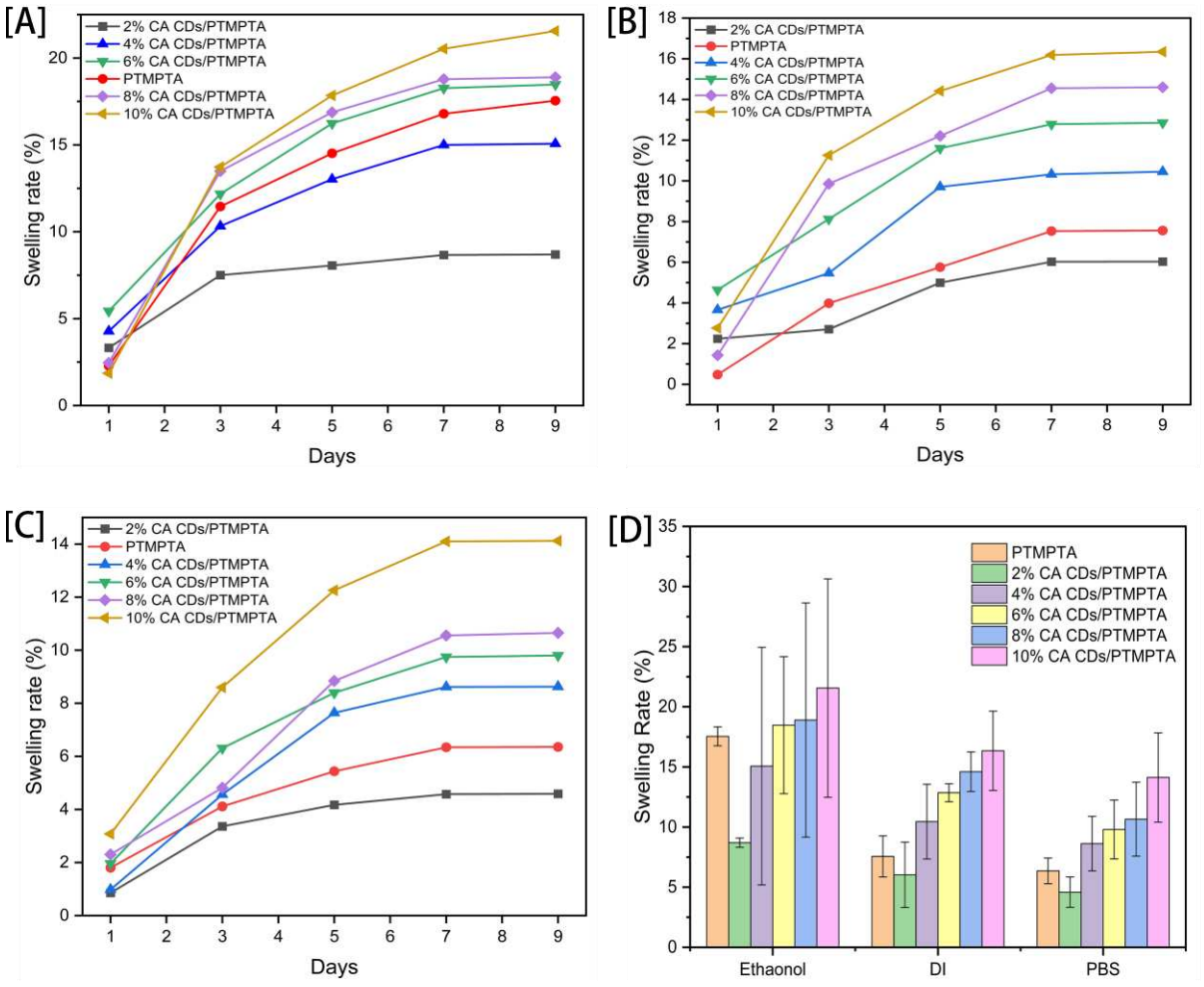

Figure S4. Changes in swelling rates of PTMPTA and CA CDs/PTMPTA composites in (A) ethanol, (B) deionized water and (C) PBS were measured within 9 days. (D): Compared the swelling rate (%) of PTMPTA and CA CDs/PTMPTA composites in ethanol, deionized water, PBS at 9 days.

Supplementary Figures and Tables

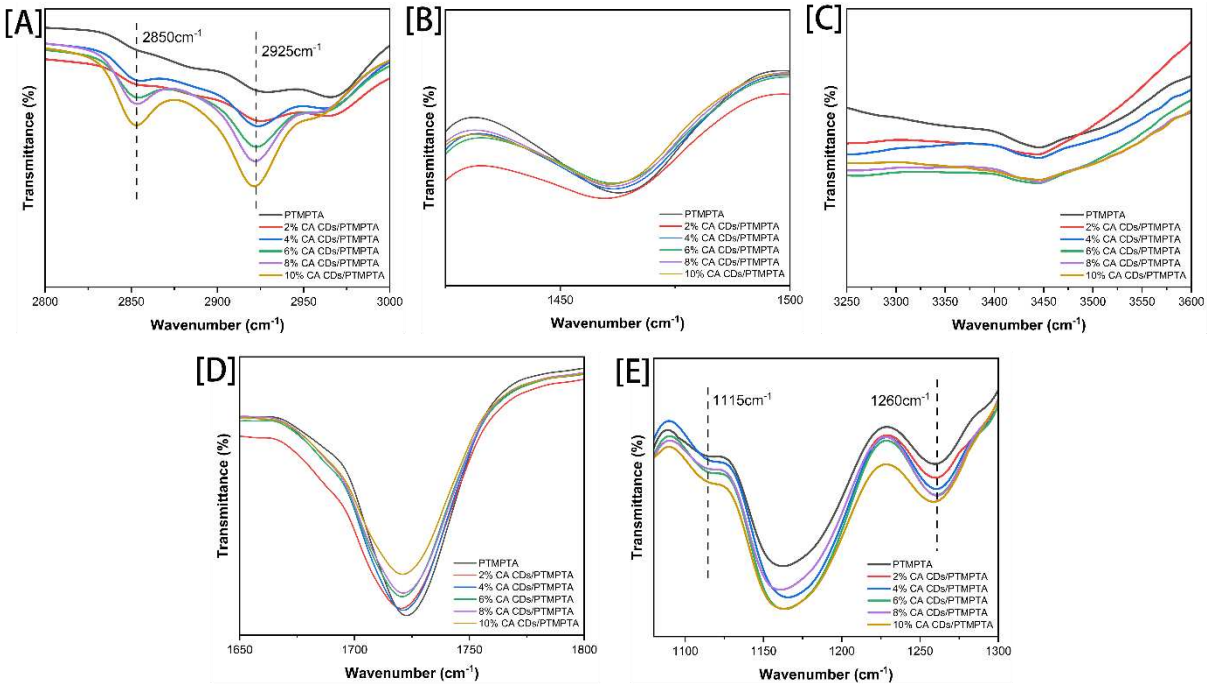

Figure S5. Partially enlarged views of the FTIR spectra of PTMPTA and CA CDs/PTMPTA composites: (A) The peaks at 2925 cm^{-1} and 2850 cm^{-1}. (B) The peak at 1460 cm^{-1}. (C) The peak at 3440 cm^{-1}. (D) The peak at 1722 cm^{-1}. (E) The peaks at 1260 cm^{-1} and 1115 cm^{-1}

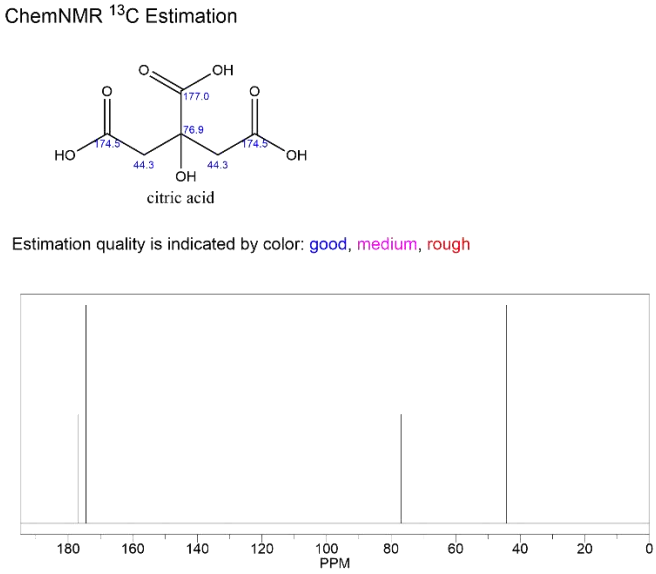

Figure S6. Predicted C NMR spectra of citric acid

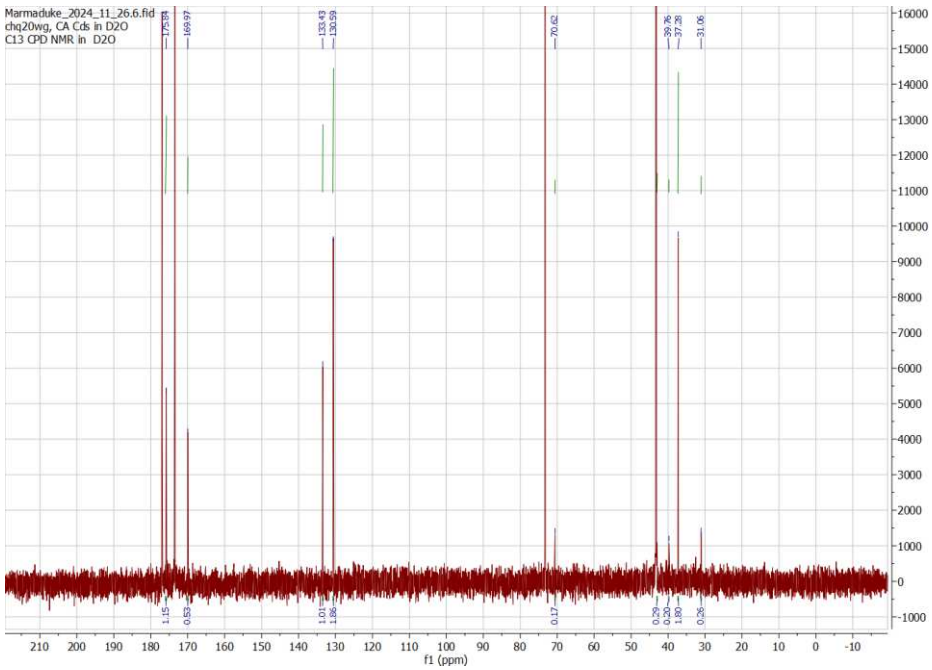

Figure S7. Integration analysis of 13C NMR of CA CDs

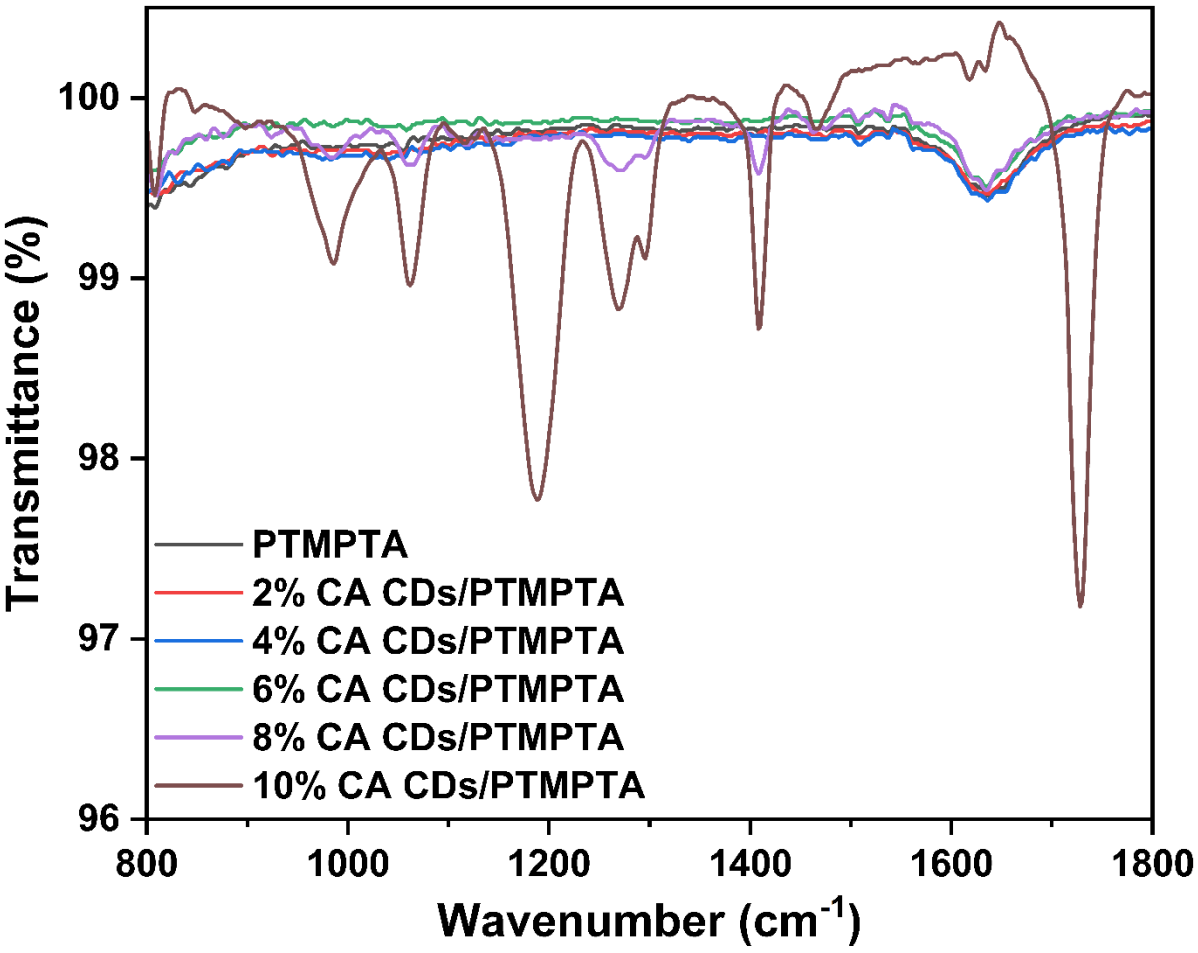

Figure S8. FTIR spectra of cell-cultured media after 7days cell viability test.

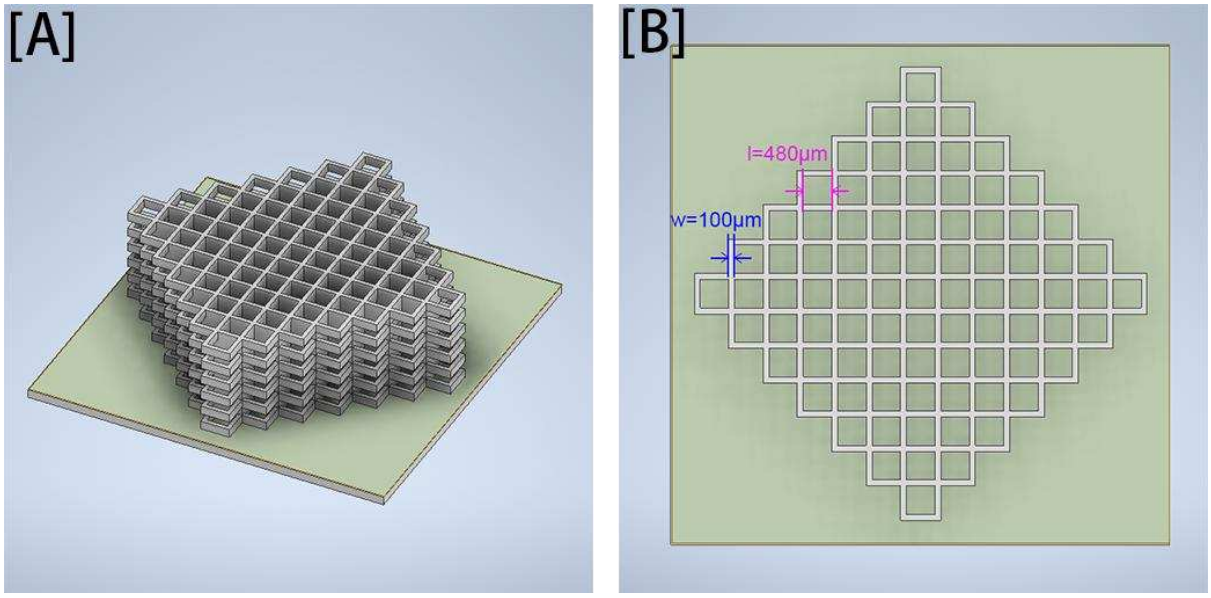

Figure S9. (A) The self-designed woodpile structure and (B) its top view, marking the square holes with a side length of 480 μm and microstructure widths of 100 μm (l × w = 480 μm × 100 μm)

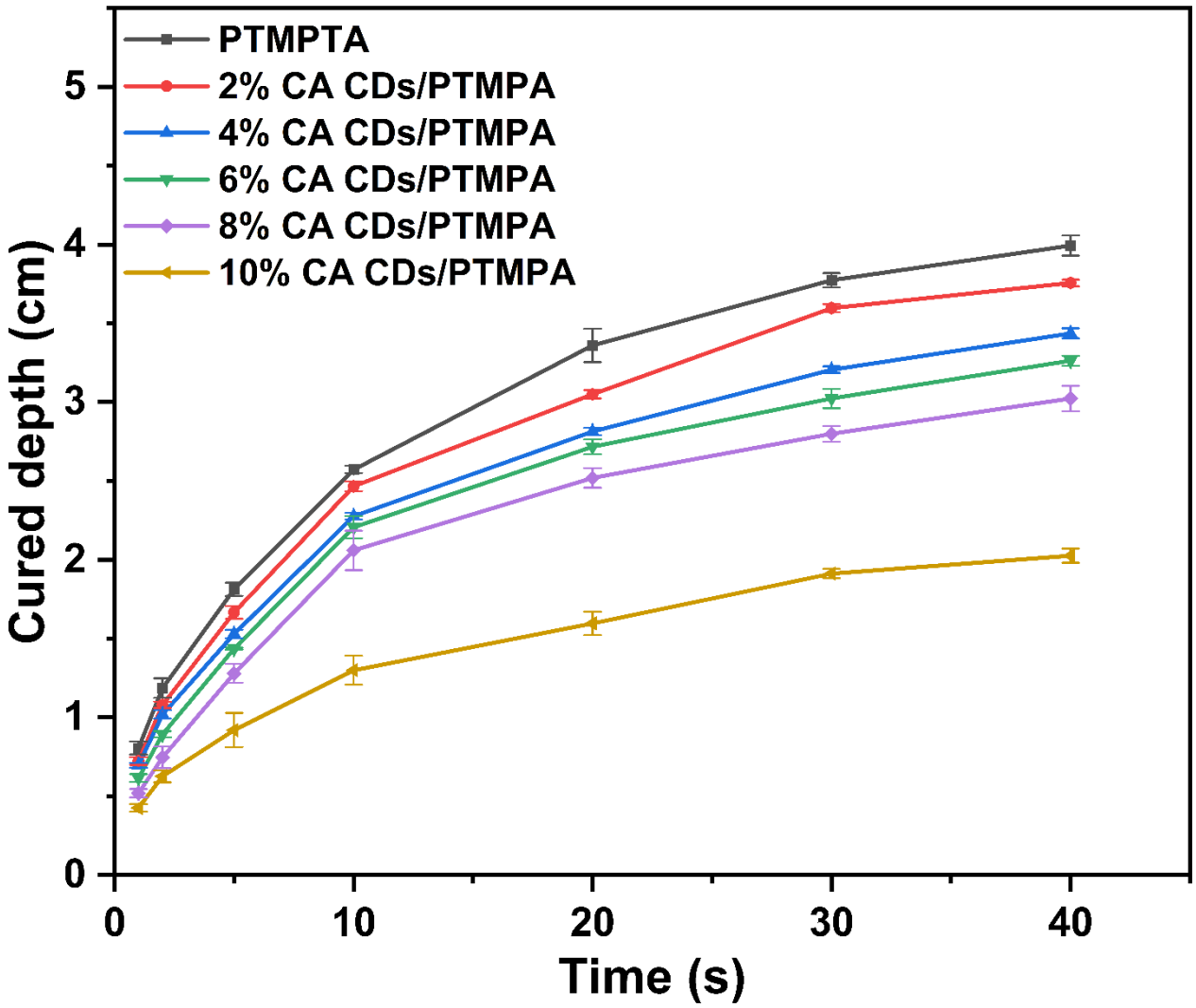

Figure S10. Photocuring depth of PTMPTA and all composites' samples upon 405 nm UV irradiation for different time. Light intensity was 700 mW/cm^2.

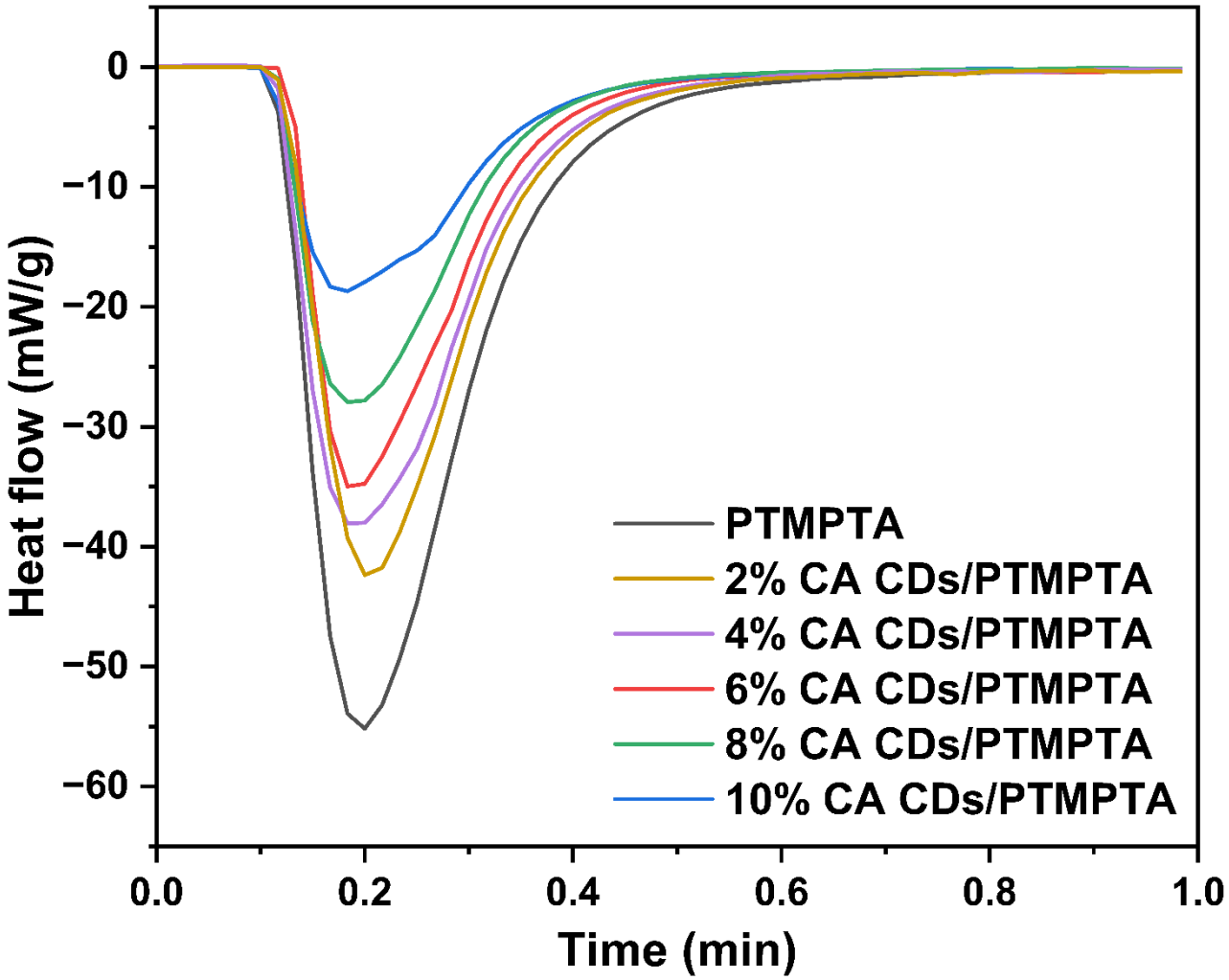

Figure S11. Photo DSC of PTMPTA and all composites prepolymer solutions under 405 nm UV light. Amount on sample in the pan was 5 mg. Measurements were taken under nitrogen. Light intensity was 700 mW/cm^2.

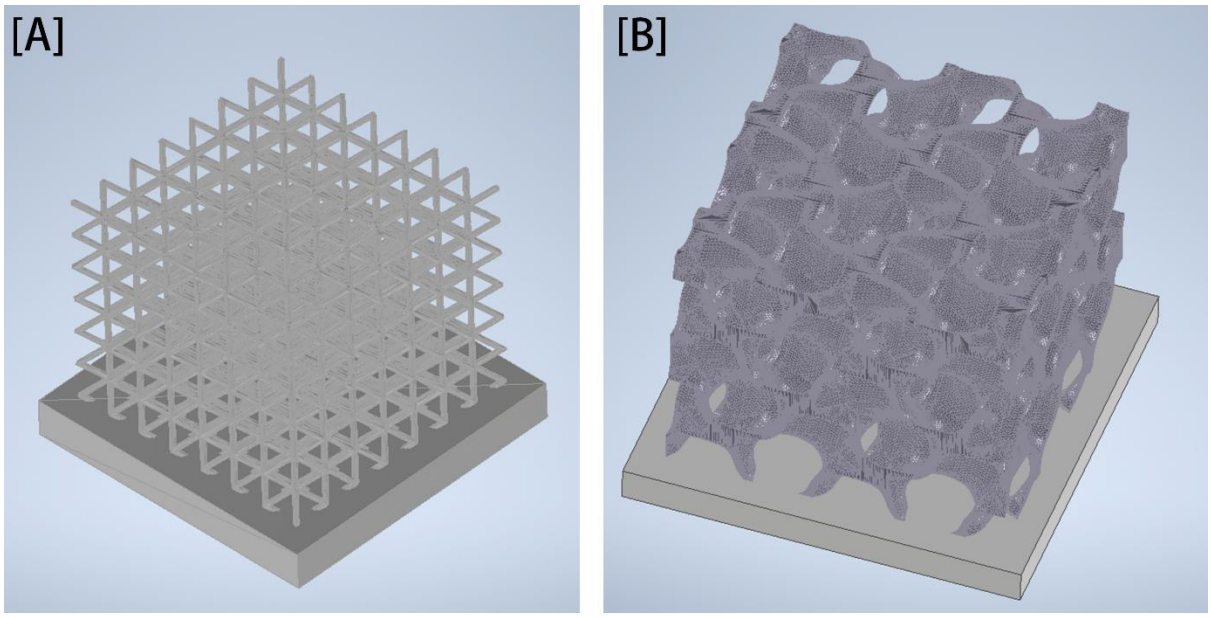

Figure S12. (A) The original cubic vertex centroid lattice structure ("lattice structure") and (B) the gyroid structure model for 3D printing

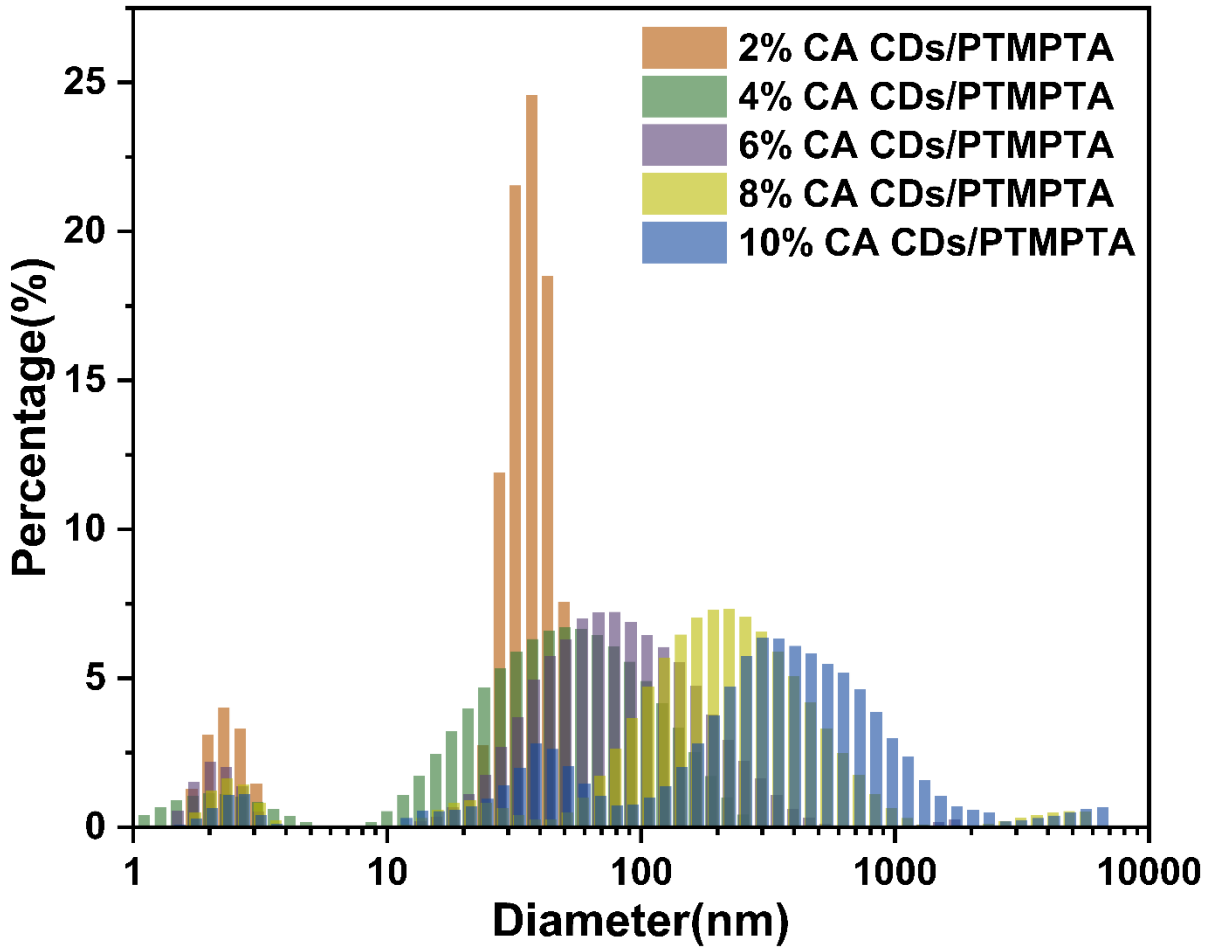

Figure S13. DLS test for particle size distribution of CA CDs in prepolymer solutions of all composites.

Table S2 Tensile Young's modulus of each sample of composites and PTMPTA

	Tensile modulus for PTMPTA (MPa)	*Tensile modulus for 2% CA CDs/PTMPTA composites (MPa)*	*Tensile modulus for 4% CA CDs/PTMPTA composites (MPa)*	*Tensile modulus for 6% CA CDs/PTMPTA composites (MPa)*	*Tensile modulus for 8% CA CDs/PTMPTA composites (MPa)*	*Tensile modulus for 10% CA CDs/PTMPTA composites (MPa)*
1	**190.735**	**306.463**	**402.373**	**416.805**	**375.452**	**351.227**
2	**294.536**	**304.931**	**360.272**	**408.506**	**364.449**	**435.849**
3	**225.065**	**307.505**	**360.207**	**430.572**	**369.063**	**437.048**
4	**244.281**	**255.516**	**340.259**	**426.368**	**336.321**	**373.452**
5	**276.05**	**280.949**	**329.314**	**390.17**	**352.765**	**380.723**
6	**234.709**	**309.963**	**363.12**	**386.996**	**375.452**	**350.761**
7	**225.05**	**285.888**	**415.844**	**355.61**	**369.063**	**430.83**
8	**232.176**	**260.207**	**365.584**	**381.189**	**358.862**	**415.499**
9	**240.777**	**294.48**	**357.282**	**444.767**	**371.426**	**341.218**
10	**244.393**	**302.835**	**309.885**	**371.22**	**364.17**	**384.15**
average	**240.7772**	**290.8737**	**360.414**	**401.2203**	**363.7023**	**390.0757**

Table S3 Compression Young's modulus of each sample of composites and PTMPTA

	Compression modulus for PTMPTA (Pa)	*Compression modulus for 2% CA CDs/PTMPTA composites (Pa)*	*Compression modulus for 4% CA CDs/PTMPTA composites (Pa)*	*Compression modulus for 6% CA CDs/PTMPTA composites (Pa)*	*Compression modulus for 8% CA CDs/PTMPTA composites (Pa)*	*Compression modulus for 10% CA CDs/PTMPTA composites (Pa)*
1	2.68767×10^{8}	4.24328×10^{8}	5.79987×10^{8}	6.79615×10^{8}	1.01637×10^{9}	4.94607×10^{8}
2	2.94933×10^{8}	4.34545×10^{8}	5.91994×10^{8}	7.70838×10^{8}	9.99498×10^{8}	1.04613×10^{8}
3	1.83065×10^{8}	4.16019×10^{8}	6.22531×10^{8}	7.4173×10^{8}	9.02662×10^{8}	1.79859×10^{8}
4	2.92963×10^{8}	4.24437×10^{8}	5.51577×10^{8}	7.88737×10^{8}	8.05973×10^{8}	1.84769×10^{8}
5	2.56002×10^{8}	4.46104×10^{8}	5.52181×10^{8}	7.11541×10^{8}	8.18884×10^{8}	1.13212×10^{8}
average	2.59146×10^{8}	4.29087×10^{8}	5.79654×10^{8}	7.38492×10^{8}	9.08678×10^{8}	2.15412×10^{8}

Table S4 Compression load-bearing capacity of each sample of composites and PTMPTA

	Compression max force for PTMPTA (N)	*Compression max force for 2% CA CDs/PTMPTA composites (N)*	*Compression max force for 4% CA CDs/PTMPTA composites (N)*	*Compression max force for 6% CA CDs/PTMPTA composites (N)*	*Compression max force for 8% CA CDs/PTMPTA composites (N)*	*Compression max force for 10% CA CDs/PTMPTA composites (N)*
1	5490	8058	10050	15599	19412	3998

2	5411	8132.9	12115	14430	17768	3358.3
3	4508.8	6990.8	12195	14785	17860	3135
4	5513.9	7098.48	9913.84	15459	20703	3835
5	6019.7	8393.3	12444.8	14737	17747.9	2263
average	5388.68	7734.696	11343.728	15002	18698.18	3317.86

Table S5 The print resolution of composites and PTMPTA

TARGET (*l* × *w*=480 *μm* × *100 μm)*	***l* (μm)**	***w* (μm)**
PTMPTA	-	-
2% CA CDS/PTMPTA COMPOSITES	-	-
4% CA CDS/PTMPTA COMPOSITES	258.2 ± 59.1	571.2 ± 74.5
6% CA CDS/PTMPTA COMPOSITES	426.8 ± 11.8	163.7 ± 15.5
8% CA CDS/PTMPTA COMPOSITES	476.3 ± 14.3	117.4 ± 13.3
10% CA CDS/PTMPTA COMPOSITES	-	-

- : Unable to replicate the designed structure.

References

[1] P. Thangaraju and S. B. Varthya, 'ISO 10993: Biological Evaluation of Medical Devices', in *Medical Device Guidelines and Regulations Handbook*, P. S. Timiri Shanmugam, P. Thangaraju, N. Palani, and T. Sampath, Eds., Cham: Springer International Publishing, 2022, pp. 163–187. doi: 10.1007/978-3-030-91855-2_11.

[2] Y. Dong *et al.*, 'Blue luminescent graphene quantum dots and graphene oxide prepared by tuning the carbonization degree of citric acid', *Carbon*, vol. 50, no. 12, pp. 4738–4743, Oct. 2012, doi: 10.1016/j.carbon.2012.06.002.

[3] X. Miao *et al.*, 'Synthesis of Carbon Dots with Multiple Color Emission by Controlled Graphitization and Surface Functionalization', *Adv. Mater.*, vol. 30, no. 1, p. 1704740, 2018, doi: 10.1002/adma.201704740.

[4] J. Guo *et al.*, 'Yellow-Emissive Carbon Dots with High Solid-State Photoluminescence', *Adv. Funct. Mater.*, vol. 32, no. 20, p. 2110393, 2022, doi: 10.1002/adfm.202110393.

[5] 'NMR Chemical Shift Values Table - Chemistry Steps'. Accessed: Dec. 02, 2024. [Online]. Available: https://www.chemistrysteps.com/nmr-chemical-shift-values-table/

[6] '13C Carbon NMR Spectroscopy - Chemistry Steps'. Accessed: Dec. 02, 2024. [Online]. Available: https://www.chemistrysteps.com/13c-carbon-nmr-spectroscopy/

[7] K. Chang, Q. Zhu, L. Qi, M. Guo, W. Gao, and Q. Gao, 'Synthesis and Properties of Nitrogen-Doped Carbon Quantum Dots Using Lactic Acid as Carbon Source', *Materials*, vol. 15, no. 2, p. 466, Jan. 2022, doi: 10.3390/ma15020466.

[8] A. Theodosiou, B. F. Spencer, J. Counsell, and A. N. Jones, 'An XPS/UPS study of the surface/near-surface bonding in nuclear grade graphites: A comparison of monatomic and cluster depth-profiling techniques', *Appl. Surf. Sci.*, vol. 508, p. 144764, Apr. 2020, doi: 10.1016/j.apsusc.2019.144764.

[9] Y. Liu, D. Chao, L. Zhou, Y. Li, R. Deng, and H. Zhang, 'Yellow emissive carbon dots with quantum yield up to 68.6% from manganese ions', *Carbon*, vol. 135, pp. 253–259, Aug. 2018, doi: 10.1016/j.carbon.2018.02.004.

[10] M. A. Sk, A. Ananthanarayanan, L. Huang, K. H. Lim, and P. Chen, 'Revealing the tunable

photoluminescence properties of graphene quantum dots', *J. Mater. Chem. C*, vol. 2, no. 34, pp. 6954–6960, Aug. 2014, doi: 10.1039/C4TC01191K.

[11] S. Zhu, Y. Song, X. Zhao, J. Shao, J. Zhang, and B. Yang, 'The photoluminescence mechanism in carbon dots (graphene quantum dots, carbon nanodots, and polymer dots): current state and future perspective', *Nano Res.*, vol. 8, no. 2, pp. 355–381, Feb. 2015, doi: 10.1007/s12274-014-0644-3.

[12] F. Oustadi, R. Imani, M. Haghbin Nazarpak, and A. M. Sharifi, 'Genipin-crosslinked gelatin hydrogel incorporated with PLLA-nanocylinders as a bone scaffold: Synthesis, characterization, and mechanical properties evaluation', *Polym. Adv. Technol.*, vol. 31, no. 8, pp. 1783–1792, 2020, doi: 10.1002/pat.4905.

[13] G. Hoti *et al.*, 'Effect of the Cross-Linking Density on the Swelling and Rheological Behavior of Ester-Bridged β-Cyclodextrin Nanosponges', *Materials*, vol. 14, no. 3, p. 478, Jan. 2021, doi: 10.3390/ma14030478.

[14] S. L. Tomić *et al.*, 'Manuka Honey/2-Hydroxyethyl Methacrylate/Gelatin Hybrid Hydrogel Scaffolds for Potential Tissue Regeneration', *Polymers*, vol. 15, no. 3, Art. no. 3, Jan. 2023, doi: 10.3390/polym15030589.

[15] R. Wang, C. Cheng, H. Wang, and D. Wang, 'Swollen hydrogel nanotechnology: Advanced applications of the rudimentary swelling properties of hydrogels', *ChemPhysMater*, vol. 3, no. 4, pp. 357–375, Oct. 2024, doi: 10.1016/j.chphma.2024.07.006.